https://doi.org/10.1016/j.jclepro.2023.136597

This is the Pre-Published Version.

Development of low-carbon alkali-activated materials solely activated by flue gas residues (FGR) waste from incineration plants

Muhammad Riaz Ahmad[1], Chandra Sekhar Das, Mehran Khan, Jian-Guo Dai[1]*

Department of Civil and Environmental Engineering, The Hong Kong Polytechnic University, Hung Hom, Kowloon, Hong Kong

Email: cejgdai@polyu.edu.hk (corresponding author)

© 2023. This manuscript version is made available under the CC-BY-NC-ND 4.0 license http://creativecommons.org/licenses/by-nc-nd/4.0/

Abstract:

Flue gas residues (FGR), a waste from incineration plant was utilized as an alternative alkaline activator to energy intensive and costly commercial activators. Fly ash (FA) and slag were used as precursors materials along with the FGR to produce low-carbon and cost-effective alkali-activated materials (AAMs). Reaction products and micromechanical properties were investigated by advanced microstructure analysis techniques. Results from the infrared spectroscopy (FTIR), thermogravimetric analysis (TGA), scanning electron microscopy (SEM) and nanoindentation indicated that reaction products were comprised of N-A-S-H gel as a major reaction product along with the hybrid gel (C-N-A-S-H) and C-A-S-H gel. SEM-EDS and nanoindentation results showed that the formation of C-A-S-H gel was directly related to content of FGR. The increase in volume of Ca-based reaction products (C-N-A-S-H and C-A-S-H) was associated with the activation of slag in presence of Na_2SO_4. Besides N-A-S-H gel, some new reaction products (zeolite, apatite and berlinite) were also observed from XRD analysis of pastes. The compressive strength of AAMs was in the range of 33.5 to 39.6 MPa and was in line with microstructure analysis results. Leaching concentrations of Ag, Ba, Cd, Cu and Zn heavy metals in FGR were 0.10, 0.40, 0.63, 0.26 and 1.65 mg/L respectively and below the regulatory limits and it was classified as a non-hazardous material.

Keywords: Flue gas residues; alternative alkaline activator; alkali-activated gel; heavy metal leaching; reaction products

1 Introduction

Production of alkali-activated binders (AABs) contributes to the utilization of local waste resources for construction materials, hazardous waste management, reduction in consumption of natural resources and carbon emissions related to OPC production (McLellan et al., 2011; Passuello et al., 2017). AABs are normally prepared by the reaction of aluminosilicate materials (e.g., fly ash, slag, metakaolin used as precursors) and a commercial alkaline activator/alkaline solution. Because of their widespread availability and relatively stable chemical properties, fly ash and slag are widely used as precursor materials (Giergiczny, 2019; Lei and Chan, 2020; Li et al., 2020; Tu et al., 2019). Hybrid AABs containing both FA and slag can form calcium-rich alkali-activated gel (C-A-S-H), geopolymer gel (N-

A-S-H) and hybrid gel (C-N-A-S-H) with the higher degree of cross-linking (Bernal et al., 2013; Perez-Cortes and Escalante-Garcia, 2020; Puligilla and Mondal, 2015; Walkley et al., 2016). The combination of alkali silicate and alkali hydroxide is normally used as the alkaline activator to produce AABs having high mechanical properties (Chen et al., 2021; Giergiczny, 2019; Shi et al., 2018; Tu et al., 2019). For the comparable mechanical performance to OPC concrete, AAB-based concrete emits 44-64% lower carbon dioxide. It has been reported that alkaline activators contribute to nearly 60% of carbon emission in AABs despite their significantly lower proportion as compared to precursors (Bajpai et al., 2020; McLellan et al., 2011; Passuello et al., 2017). The preparation process of these alkali silicate activators involves heating the silica and sodium bicarbonate at elevated temperatures which not only releases a high amount of carbon dioxide thus polluting the environment but also produces activators with a high cost and high embodied energy (Fawer et al., 1999). To further reduce the cost and environmental impact of AABs, finding a cost-effective activator with low embodied energy is necessary.

In this regard, researchers have synthesized sodium silicate using amorphous silica and sodium hydroxide by hydrothermal process. Rice husk ash, silica fume, waste glass powders have been identified as amorphous silica sources to prepare the sodium silicate while sodium hydroxide is used as a source of alkali metal (Alnahhal et al., 2021; Geraldo et al., 2021). The nature of reaction products in AABs prepared by synthesized activators and commercial activators was similar. Activators prepared by hydrothermal and thermomechanical methods possess some limitations. The corrosive nature of alkaline activator prepared through hydrothermal method at elevated temperature of 150-250℃ can damage the pressure reactor vessels (di Bella et al., 2003). Whereas, a significantly lower amount of silica is dissolved at a lower temperature <100℃, hence producing the activators resulting in AABs having lower mechanical properties (Puertas and Torres-Carrasco, 2014; Torres-Carrasco and Puertas, 2015). In the thermomechanical process, synthesis is performed at significantly higher temperatures (500-1300℃) which can dissolve a higher amount of silica. However, prepared activator needs reheating at higher temperature (175℃) before use due to its lower solubility at room temperature (Hu et al., 2015; Keawthun et al., 2014; MORI, 2003). Some other studies have reported the use of cleaning solution (Fernández-Jiménez et al., 2017), waste glass powder (Keawthun et al., 2014; Vinai and

Soutsos, 2019a, 2019b), bottom ash (Maldonado-Alameda et al., 2021) and sugarcane straw ash (Moraes et al., 2018) in conjunction with the sodium hydroxide to prepare the alternative alkali silicate activator. In this study, a highly alkaline industrial waste known as "Flue gas residues (FGR)" transported from the incineration plant was solely used as a source of alkaline activator to prepare the hybrid alkali-activated fly ash slag pastes.

FGR is produced as waste residues during the treatment of sewage sludge at incineration plants (or waste to energy, WtE plants) and obtained on the downstream side after the flue gas treatment process (Ahmad et al., 2023, 2022). It is of highly alkaline waste and corrosive in nature and contains soluble ions and potentially toxic elements. After storing the FGR at the plant facility temporarily, it is sent to landfill sites for disposal purposes. The yield of FGR is estimated in the range of 2-6% of total waste burned at incineration plants (Bogush et al., 2015). At present, Hong Kong has a sewage sludge treatment plant that can incinerate approximately 2000 tonnes of sewage sludge per day. Soon, Hong Kong will also complete the construction of a new MSW treatment plant (WtE plant) in 2025 which will be able to treat 3000 tonnes of MSW per day (EPD, 2021). As Hong Kong government is eager to reduce the net carbon footprint to zero in waste management and phase out landfills gradually, recycling of incineration ashes from WtE is of high priority to achieve the sustainability goals.

Regarding the recycling of FGR, very few studies have explored the use of FGR as construction material (Bogush et al., 2020; Quina et al., 2014; Stegemann, 2014). FGR has been used to prepare the precursors for AAB using DC plasma technology along with the glass forming additives (Kourti et al., 2010). AAB having low compressive strength (<10 MPa) was prepared using the fuel ash and FGR using the waste caustic solution containing alumina (Shirley and Black, 2011). Opposite to other precursors like FA and slag, the chemical composition of FGR can show significant variations depending upon the treatment process and hence poses several challenges for its usage in the construction industry. One way to avoid large differences in chemical composition of FGR is to use the same type of waste for incineration. This process would ensure the production of FGR with fairly similar composition. Another way to reduce differences in chemical composition is to establish national or international standards for the incineration process and the disposal of flue gas residues. These standards could specify the types of

waste materials that can be used for incineration, the operating conditions for WtE plant, and the regulatory limits of specific chemicals, such as heavy metals. Authors have identified the high content of alkalis (Na) from the chemical composition of the FGR obtained from the incineration plants in Hong Kong. The use of FGR as an alkali-activator (due to its highly alkaline content) could potentially contribute to the further enhancement of sustainability of AABs as alkali-activator is the major source of carbon emitter and most expensive material in the preparation of AABs (Ahmad et al., 2023; Qian et al., 2023).

The main objective of this study is therefore to introduce the FGR as the sole activator to produce the hybrid fly ash/slag-based AABs through the alkali-activation phenomenon. The production of AABs using FGR as a sole activator will have significant impact as FGR will not only improve the sustainability of AABs by cutting down the carbon emission and cost of commercial alkaline activator but will also amplify the waste resource utilization and reduce environmental risk associated with the leaching of heavy metals in FGR. AABs were prepared with the FGR to precursors ratio of 0.24, 0.32 and 0.40, respectively. The leaching characteristics of FGR were checked for heavy metals regulatory limits and FGR was categorized as non-hazardous material. The characterization of AABs was conducted through a detailed study including the compressive strength, hydration mechanism and microstructure analysis using XRD, TGA, FTIR, SEM-EDX and nano-indentation analysis techniques.

2 Materials and Methods

2.1 Raw materials

Raw materials used in this study to prepare AAB include fly ash (FA), slag and FGR. FA was transported from the local power plant (CLP) in Hong Kong and Slag was purchased from mainland China. FA and slag were used as received without any treatment. FGR was acquired from the WtE plant (T-park) in Hong Kong. The particle size distribution (PSD) of finely ground FGR, raw FA and slag is provided in Fig. 1. The average diameter (D50) of FGR, FA and slag was 7.0, 20.1 and 14.1 μm respectively. Chemical composition of raw materials was determined by X-ray fluorescence (XRF) emission method using Rigaku supermini 200 apparatus. The results of chemical analysis are shown in

Table 1. FA falls into Class-F with low-calcium content and percentage of SiO_2, Al_2O_3, and Fe_2O_3 combined was higher than 80% by mass. Dominant phases in FGR were Na_2O (38.3%) and SO_3 (31.9%). The higher percentage of alkalis in FGR could support the chemical reaction to produce the alkali-activated materials. Slag and FA particles were of angular shape and sphere shape respectively as shown in SEM images (Fig. 2). FGR consisted of fluffy and partially rounded shaped particles.

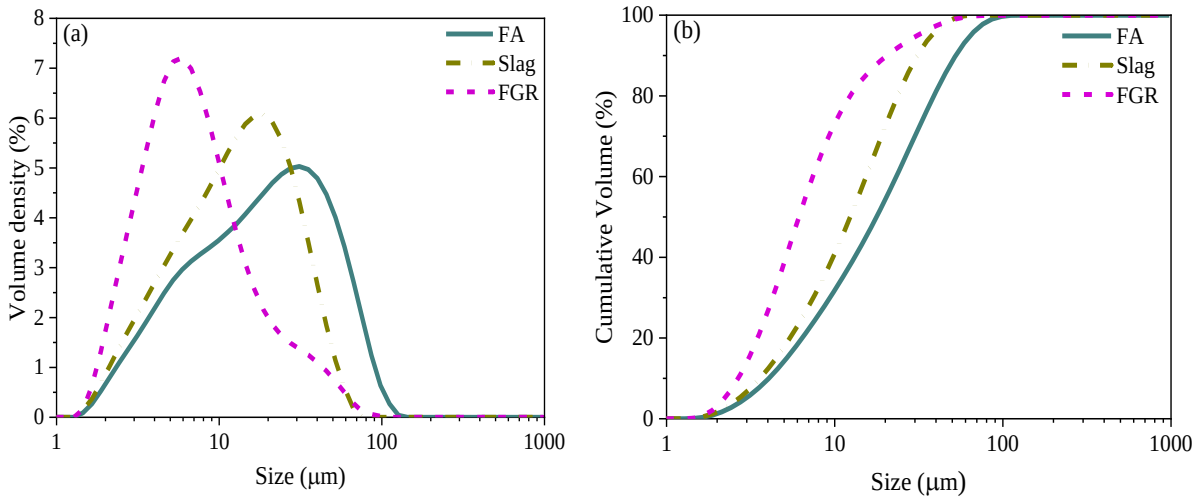

Fig. 1. PSD analysis of raw materials (a) volume density of FA, slag and FGR and (b) cumulative volume of FA, slag and FGR

Table 1. Chemical composition of FA, slag and FGR (% by mass)

Oxides	SiO_2	Al_2O_3	Fe_2O_3	CaO	MgO	Na_2O	K_2O	TiO_2	P_2O_5	SO_3	Others
Fly ash	49.7	25.1	9.58	7.84	2.8	-	1.53	1.15	0.84	0.96	0.5
slag	32.6	14.7	0.35	42.4	6.53	-	0.41	0.61	0.18	1.82	0.4
FGR	6.19	3.57	4.65	3.27	1.71	38.3	0.57	0.19	3.02	31.9	6.64

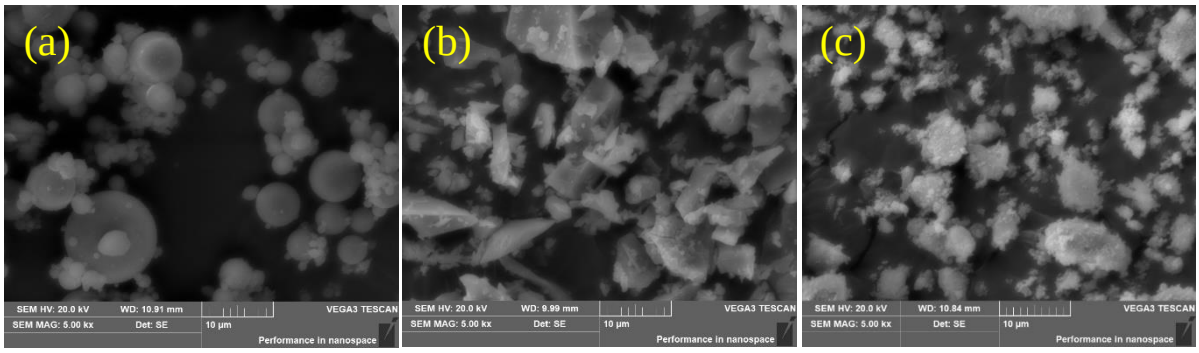

Fig. 2. SEM images of raw materials (a) FA, (b) slag and (c) FGR

2.2 Sample preparation method

2.2.1 Preparation of FGR to use as an alkaline activator

After transporting to laboratory, FGR lumps were dried in an oven for 24 hours at a constant temperature of 105℃. After drying, FGR was finely ground in a ball mill machine for 4 hours. The weight of steel ball and FGR in milling machine was 12 and 4 kg, respectively. Before preparing the paste mixtures, FGR was dissolved into the deionized water to prepare FGR based alkali-activator solution. The ratios of FGR to deionized water were 0.65, 0.81 and 0.95 respectively to prepare the FGR-0.24, FGR-0.32 and FGR-0.40 AAB pastes. Hence, this simple process prepares the FGR-based alkaline activator which was used later as a liquid alkali-activator to produce the AAB pastes.

2.2.2 Mixing method

Three AAB pastes were produced by mixing the FA, slag and FGR. The ratio of FA to slag was kept 0.7:0.3. The higher percentage of FA could increase the utilization rate of FA and reduce production cost of AAMs whereas 30% slag provides sufficient compressive strength to the matrix for practical applications due to its high reactivity as compared to FA. The source of alkali was supplied by the waste-derived based FGR activator. Mix proportions of three pastes are provided in Table 2. The ratio of FGR to precursor for three pastes was 0.24, 0.32 and 0.40 respectively and hence the mixtures are designated as FGR-0.24, FGR-0.32 and FGR-0.40 respectively, indicating the amount of FGR in each mixture. Based on the amount of FGR, alkali contents (Na_2O) were 9.20%, 12.26% and 15.32% of total precursors. The FGR solution to precursor ratio for all mixtures was 0.30.

During the mixing procedure, FA and slag precursors were mixed in the dry condition in a mortar mixer at slow speed. After dry mixing for 5 minutes, FGR based liquid activator solution (as detailed in section 2.2.1) was introduced into the dry mixed precursors to prepare the AAB slurry paste. The wet mixing was carried out for 10 minutes until homogenous mixture with good workability was obtained. Fresh AAB pastes were transferred into molds of 40 × 40 × 40 mm^3 size. The fresh pastes were placed on a vibrator to remove air bubbles and for compaction purpose. The molds were then wrapped with plastic sheets and were placed in an electric oven at a fixed temperature of 80℃ for 72 hours. It is important to mention that the reactivity of FGR based activator is very low at the ambient conditions so heat curing

was adopted to obtain the AABs having high strength. After 3 days of heat curing, samples were cooled down to ambient temperature in oven for 24 hours, demolded and tested for compressive strength and microstructural properties.

Table 2. Mixture proportions of FGR-AABs

Mix ID	Slag:FA	FGR/Precursor	FGR-activator solution/precursor	Na_2O/Precursor (%)
FGR-0.24	0.3:0.7	0.24	0.30	9.2
FGR-0.32	0.3:0.7	0.32	0.30	12.3
FGR-0.40	0.3:0.7	0.40	0.30	15.3

2.3 Experimental methods

Phase characterization of AABs was performed by testing the samples for the thermogravimetric analysis (TGA), Fourier transform infrared spectroscopy (FTIR), x-ray diffraction (XRD), nano-indentation and scanning electron microscopy-energy dispersive analysis (SEM-EDS). The samples for the phase characterization were taken from the inner core of cubic specimens. The small pieces of samples were soaked in absolute alcohol for 7 days to stop hydration reaction. After that samples were dried in a vacuum oven at a constant temperature of 40°C.

2.3.1 TGA analysis

After drying, the samples for the XRD, FTIR and TGA analysis were manually ground to fine powder by the pestle and mortar and passed through the sieve no. 75 µm. TGA test on AABs powder samples was performed under argon gas environment by Rigaku Thermo Plus EVO2 apparatus. Powder samples for TGA were weighed in aluminum crucible. The mass of samples varied between 10-15 mg. The samples were heated at the rate of 10°C/min starting from the temperature 30°C to 1000°C. The measurement time for each sample was around 2 hours.

2.3.2 XRD analysis

For the phase characterization, XRD analysis was conducted by Rigaku SmartLab Advance machine under the Bragg-Brentano mode. The powder samples were placed in a glass sample holder by the front-loading method. The conditions for the XRD tests were as follows (scanning rate: 0.02°, current: 20 mA, voltage: 45 kV, 2θ value from 10° to 70° and Cu-Kα radiations). The measurement time for each sample was around 10 minutes.

2.3.3 FTIR analysis

FTIR test was performed on the AABs samples for the identification of different functional groups. The test was conducted by PerkinElmer UATR-two instrument at a resolution of 2 cm^{-1} and wavenumber ranging from 400 cm^{-1} to 4000 cm^{-1} in the absorption mode.

2.3.4 SEM-EDS analysis

For the SEM-EDS and nano-indentation tests, small pieces of AAB pastes were first placed into fresh epoxy and air bubbles were removed through the vacuum chamber. After the setting of epoxy, samples were demolded and polished by grinding and polishing apparatus (model: Buehler, AutoMet 300). Grinding and polishing were carried out in four steps. In the first step, epoxy was ground to a flat surface using Grit 600 by using water as a lubricant until surface of sample is exposed. Samples were then cleaned in the ethanol in an ultrasonic bath for 5 minutes at 25°C. The last three steps were related to the polishing of samples. Polishing of samples was completed by using the 9µm, 5µm and 0.05 µm grits (diamond/alumina grits) and their corresponding MetaDi diamond suspensions. Polishing time for each grit was 5 minutes. After each polishing step, samples were immersed into ethanol and cleaned using ultrasonic bath to remove any dust particles on sample surface. After polishing was completed, samples were transferred to a vacuum oven for drying purpose. The temperature of vacuum oven was set to 40°C. SEM analysis was performed by Tescan Vega 3 XMU machine which was equipped with the EDS facility. The samples were fixed on the stubs and coated with a thin layer of carbon. The point analysis on samples were performed at different 50 different locations for the characterization of unreacted and reacted phases through statistical analysis of elemental ratios. The analysis was performed at a working distance of 15 mm and an accelerating voltage of 20kV under high vacuum conditions.

2.3.5 Micromechanical testing

The sample preparation and polishing procedure of samples for the nano-indentation test was similar to SEM test, however, time for each polishing step lasted 30 minutes to achieve a highly smooth surface. Nano-indentation test was conducted by TI 950 TriboIndenter by Burker. The surface roughness of AAB samples was tested by scanning probe microscopy (SPM) on the grid area of 50 µm × 50µm. The

surface roughness profile of each sample measured by SPM is shown in Fig. 4. After determining that the roughness of samples is suitable to perform the nano-indentation, a square grid was selected for the indentation purpose. In total, 121 points (11 × 11) were chosen with a gap of 5 μm between two adjacent grid points. Loading and unloading of samples were conducted by a trapezoidal loading profile. The loading rate was 400 μN/s and 2000 μN was selected as peak load limit. The peak load was maintained for 2 s and then samples were unloaded at the same rate as loading. The test at the one grid was completed in 7 hours.

2.3.6 Compressive strength

Compressive strength test on FGR alkali-activated pastes was performed after the heat curing using compression strength testing machine (MATEST 3000 kN). The specimens were left in oven to cooled down to ambient temperature after heat curing. The size of specimens for compressive strength was 40 × 40 × 40 mm^3. The dimensions of samples surface exposed to compression platens were measured to calculate the loaded surface area. The loading rate was kept at 0.6 MPa/s for all samples. The average value of compressive strength was reported by testing the six samples for each cement paste.

2.3.7 Micro X-ray tomography (Micro-CT)

The 3D images of FGR-AAMs were observed by Micro -CT Bruker Skyscan 1276 machine to study the porosity and microstructure. The current and voltage of X-ray tube were maintained at 200 μA and100 kV and during the observation. The cubic shape samples of 15 mm in size were used for micro-CT scanning. The scanning was performed at 7 μm to analyze the distribution of pores. The size of reconstructed images was selected as 5 × 5 × 5 mm^3 cubic shape.

2.3.8 Heavy metal concentration and leaching test

The total concentration of heavy metals was determined by digesting the FGR sample through the aqua-regia digestion method. Digested samples were tested by inductively coupled plasma-optical emission spectrometer (ICP-OES). The leaching test on FGR was performed by synthetic precipitation leaching procedure (SPLP) following the US EPA method 1312 (Method 1312, 1994) and toxicity characteristics leaching procedure (TCLP) following the US EPA method 1311 (Us, 1992) respectively. Two different extraction liquids were used in these leaching tests. The purpose of SPLP test was to explore the

leaching potential of heavy metals from FGR in the event of acid rain and TCLP method determines the leaching of heavy metals in FGR when used for landfilling and remediation purposes. Glacial acetic acid was used as an extraction liquid in both tests. The weight ratio of FGR powder sample and extraction liquid was 1:20. The samples along with the extraction liquid were rotated in capped polypropylene bottles at 30±2 rpm for 18±2 h. Filtrate of dissolved FGR was obtained by passing the liquid through the glass fiber filter of 0.45 μm diameter. Filtrate samples were further digested, diluted and tested for the leaching concentration by ICP-OES.

3 Results

3.1 FTIR analysis

The results of FTIR spectroscopy conducted on the raw precursors and AAM pastes are shown in Fig. 3. The position of main band of reaction products was concentrated at 987-988 cm^{-1} (Fig. 3b) and is attributed to asymmetric stretching vibration of Si-O-M bond (M = Si or Al). The main band was present at 1054 cm^{-1} for FA precursor and 900 cm^{-1} for slag (Fig. 3a). The shift of main band in geopolymer pastes was due to reaction of the raw precursors and FGR which caused the dissolution of aluminosilicate materials and formed the reaction products (geopolymer or alkali-activated gels, T-A-S-H, T = Ca or Na) in the presence. During the reaction, Si is gradually substituted with Al as bond forces are weaker in Si-O-Al as compared to Si-O-Si and inherent structure of aluminosilicate-based precursors is depolymerized. As the reaction progresses, Si/Al of tetrahedral Si sites are decreased continuously and more reaction products are precipitated. Initially, these sites are surrounded by Al atoms and reaction products (T-A-S-H gels) are formed as tetrahedrally linked Si and Al atoms are bridged between the oxygen atoms due to dissolution of Al (Granizo et al., 2014; Zhang et al., 2012). Hence, the main band present in original precursors is shifted due to formation of reaction products.

FTIR results also show the appearance of new absorption peaks around 614, 638 and in the range of 1083-1102 cm^{-1}. It is worth noting that the intensity of these peaks is significantly increased when amount of FGR is increased from 24% to 40%. The peak around 615 cm^{-1} is associated with the asymmetrical bending vibration of SO_4^{-2} bond (Das et al., 2014) originated from the FGR and the weak

peak at 638 cm^{-1} is linked to symmetrical stretching vibration of Si-O bond (Lee and van Deventer, 2002). In the raw FA, a very low shoulder peak is present around 1095 cm^{-1} due to asymmetric stretching vibration of Si-O bond linked to Q^3 sites. When FGR is added into precursors this peak became more apparent and shifted its position to a lower wavenumber of 1083 cm^{-1} in FGR-0.24. With the further increase in FGR to 32% and 40%, the intensity of this peak is further increased and is shifted to higher wavenumber 1087 cm^{-1} and 1102 cm^{-1} in FGR-0.32 and FGR-0.40 respectively. This peak is associated with the presence of phases which are rich in silica and contains some amount of alkalis and calcium (García-Lodeiro et al., 2008; Lodeiro et al., 2009).The appearance of this peak is due to anti-symmetric stretching vibration of sulfate (SO_4^{2-}) bond as a result of addition of FGR which contains high amount of Na_2SO_4 (Li et al., 2012). The peaks around 1473 cm^{-1} and 878 cm^{-1} show the presence of O-C-O bonds (due to asymmetric stretching) in CO_3^{2-}. These peaks are associated with the carbonation of paste powder during the preparation process. The common band in raw FA and pastes in the range of 446-448 cm^{-1} is present which is linked to vibration of Si-O due to the presence of quartz (Yang et al., 2022).

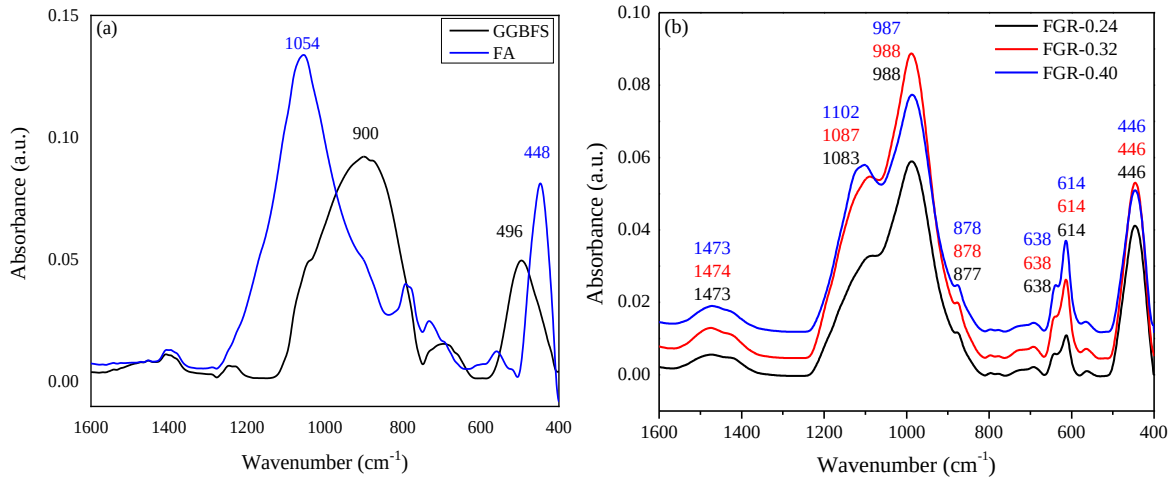

Fig. 3. FTIR results of AAMs activated by FGR

3.2 X-ray diffraction analysis

X-ray diffractograms for the FGR and precursors (FA and Slag) are shown in Fig. 4a. The phases present in raw FA were mainly quartz and mullite. Slag consisted of amorphous nature phases which are represented by a broad hump from 25-35. FGR was comprised of trisodium phosphate (Na_3PO_4), thenardite (Na_2SO_4), hematite (Fe2O3), leucite ($KAlSi_2O_6$) and monosodium phosphate (NaH_2PO_4)

(Ahmad et al., 2022). The results of XRD analysis for AAMs pastes are provided in Fig. 4b. At the lower content of FGR, peaks of Na_2SO_4 were absent showing its complete dissolution due to its lower content. The intensity of peaks for thenardite (Na_2SO_4) and halite (NaCl) increased with the increase in percentage of FGR. The presence of thenardite peaks shows that there might be some amount of residual Na_2SO_4 when amount of FGR and it did not completely react in AAM system and recrystallization of excessive Na_2SO_4 occurred when cement paste hardened. There were no major differences in the peak intensity of quartz, mullite and hematite for all pastes showing inert behavior of two phases. These phases originate from the FA and FGR as can be observed from the XRD pattern and chemical composition of these materials. The presence of C-(A)-S-H gel is observed at 29° 2θ. However, this peak is also linked to calcite ($CaCO_3$) and was present in all FGR-AAM pastes. The formation of calcite could occur during the sample preparation process. Some traces of apatite are also found which is calcium phosphate, which could be precipitated in an alkaline environment due to the reaction of Ca^{2+} from slag and PO_4^{3-} from FGR. Its effect on the mechanical properties of AAMs is limited due to the limited amount of PO_4^{3-} in FGR (Pangdaeng et al., 2015).

The visible broad hump in FA (20-32° 2θ) shows the amorphous nature of precursors and it consists of aluminosilicate phases which influence the reactivity of FA precursors as it helps to form the zeolite or geopolymers. After adding the FGR, this glassy phase of FA and broad hump in slag (25-35° 2θ) is converted to amorphous aluminosilicate reaction products (N-A-S-H/C-N-A-S-H) along with the fabrication of zeolite phases as secondary hydration products. The primary reaction product in all AAMs is N-A-S-H gel and can be observed through a broad hump centered at 30° 2θ (Lv et al., 2020; Moutaoukil et al., 2022; Wang et al., 2022). A new phase called berlinite ($AlPO_4$) appears in all paste samples. The formation of berlinite is due to the reaction of phosphate from FGR and alumina from the FA precursor in a basic pH environment. It has been reported that berlinite formed during geopolymer reaction can act as a filler and improve the mechanical properties of pastes (Moukannaa et al., 2019; Tchakouté et al., 2021).

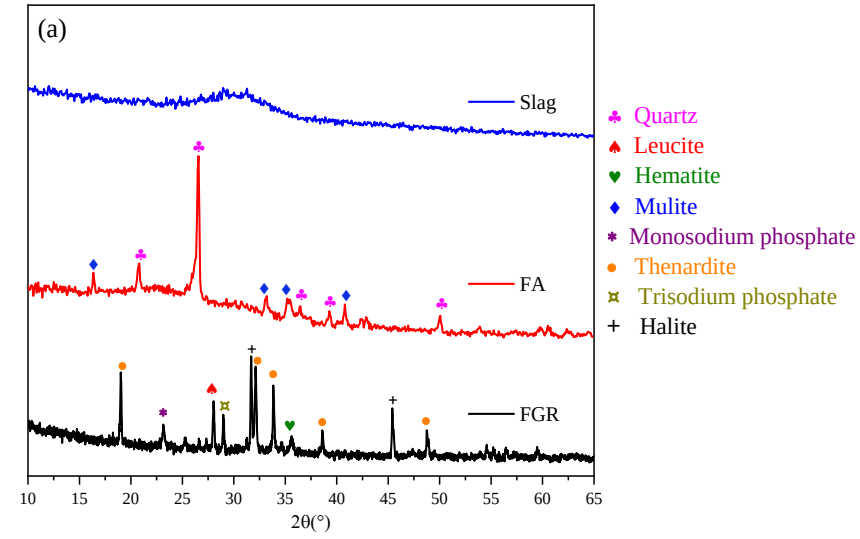

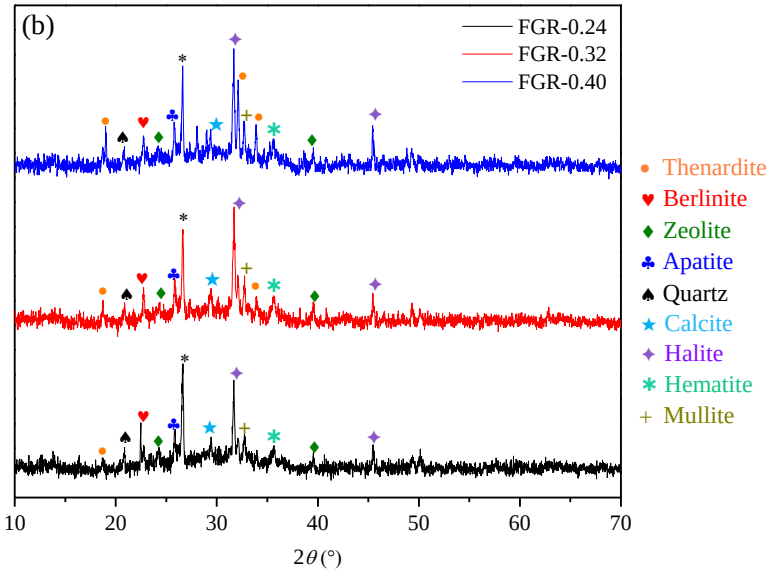

Fig. 4. Study of mineral phases and hydration products by XRD analysis for (a) raw materials and (b) FGR-activated pastes

3.3 Thermogravimetric analysis (TGA)

The results of TGA analysis performed on AAMs are presented in Fig. 5. The change in mass loss with the increase in temperature from 30°C to 1000°C is shown in Fig. 5a and encircled in DTG curves as plotted in Fig. 5b. The mass loss in different temperature ranges can be associated with the different type of reaction products and is shown in Fig. 5c. The early loss in mass at low temperature (in range of 40-160°C) is associated with the evaporation of physically bound and free water in N-A-S-H gel (Kuri et al., 2021). A substantial loss in mass was observed in this temperature range. The water

associated with N-A-S-H gel is completely removed at 300℃ (Rafeet et al., 2019). The mass loss for the FGR-0.24 was highest (4.78%) in this range and closely followed by the FGR-0.32 (4.74%) and FGR-0.40 (4.69%) respectively. The mass loss in the range of 300-600℃ is attributed to the dehydration of calcium-based reaction products (C-A-S-H, C-(N)-A-S-H) with some Na ions in their structure. The mass loss in range of 300-600℃ was lowest for FGR-0.24 paste which was slightly increased when amount of FGR was increased, showing that a slightly higher volume of C-A-S-H gel was formed when the contents of FGR were higher. The loss in mass up to 600℃ is an indirect indication of reaction degree of AAMs (Rafeet et al., 2019), which was 6.89%, 6.97% and 6.89% for the FGR-0.24, FGR-0.32 and FGR-0.24 respectively. Hence, reaction degree was slightly higher for FGR-0.32 paste as compared to FGR-0.24 and FGR-0.40 pastes. The third mass loss hump ranged from 675℃ to 775℃ with the peak concentrated around 720℃ and linked to the decomposition of calcite ($CaCO_3$) into CO_2 and CaO. The presence of carbonation products was also identified in FTIR and XRD analysis. There was a sharp increase in mass loss after 800℃ in all paste samples. The mass loss after this range increased with the increase in amount of FGR. The increasing trend of mass loss in this range is due to evaporation and melting of soluble salts (Na, K, Ca) containing chloride and sulfate ions (Amutha Rani et al., 2008; Bogush et al., 2019).

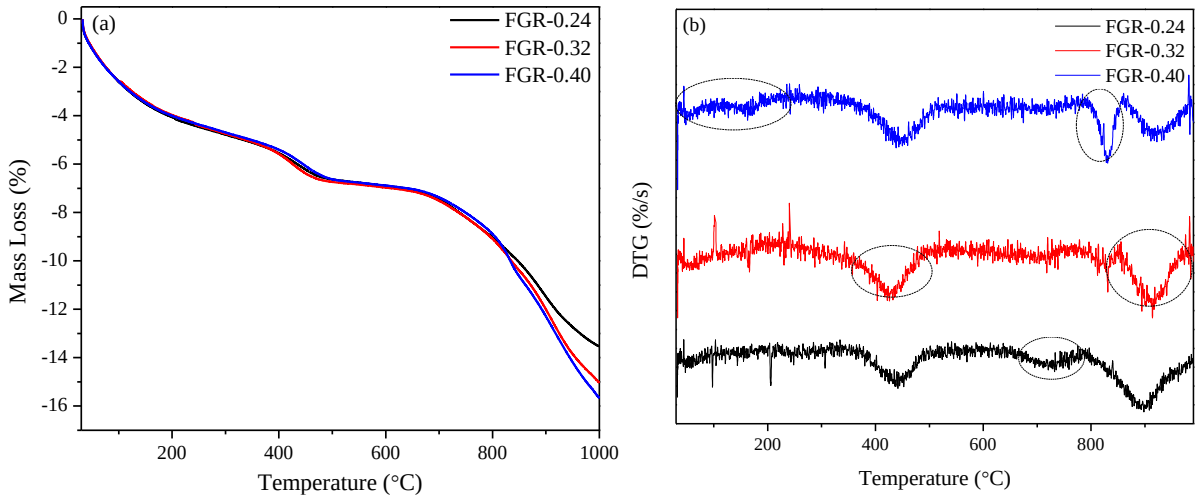

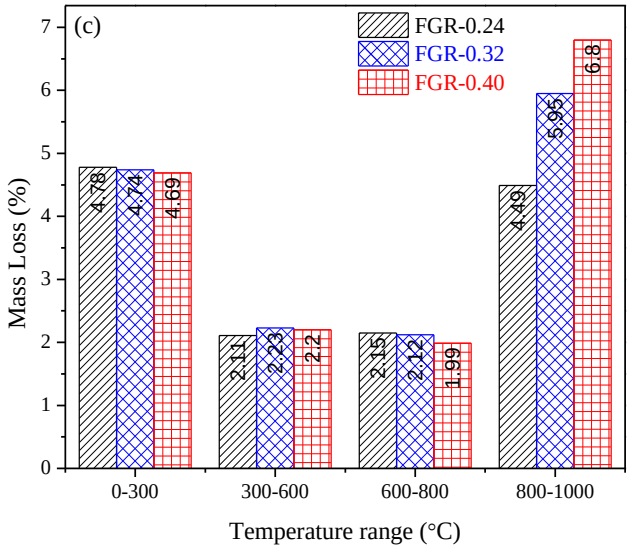

Fig. 5. TGA analysis of AAMs activated by FGR

3.4 SEM-EDS analysis

SEM BSE images of polished AAM samples are provided in Fig. 6 and EDS analysis results on the different area of samples are given in Table 3. The EDS analysis was performed on several areas for each sample to identify the different reaction products, partially reacted or unreacted phases. For each AAM paste, 6 areas are highlighted in yellow rectangles. The composition of only major elements (Ca, Al, Si and Na) participating in the reaction is presented in Table 3. The first area in all pastes showed the presence of geopolymer gel (N-A-S-H) along with the presence of Ca phases in lower quantities. In area 2, Ca, Al and Si elements were present in dominance revealing the formation of alkali-activated gel Ca rich gel (C-A-S-H). The cross-linked reaction products N-(C)-A-S-H and C-(N)-A-S-H with the equivalent proportion of Na and Ca were found in area 3 and 4 respectively. In area 5, EDS analysis was performed on the slag particles in pastes. It can be observed that Ca/Si ratio of slag particles in FGR-0.24, FGR-0.32 and FGR-0.40 was reduced to 1.10, 1.26 and 1.18 respectively as compared to raw slag (Ca/Si = 1.99). It shows that residual slag particles present in pastes have reacted partially as some of the Ca^{+2} ions were leached out. EDS analysis in area 6 was conducted on the FA particles that have participated in the reaction and are partially dissolved in pastes to form reaction products. The Si/Al of these reacted FA particles was significantly reduced than that of raw FA (1.75) as vitreous phases of Si are released and react in the presence of an FGR activator to form the reaction products.

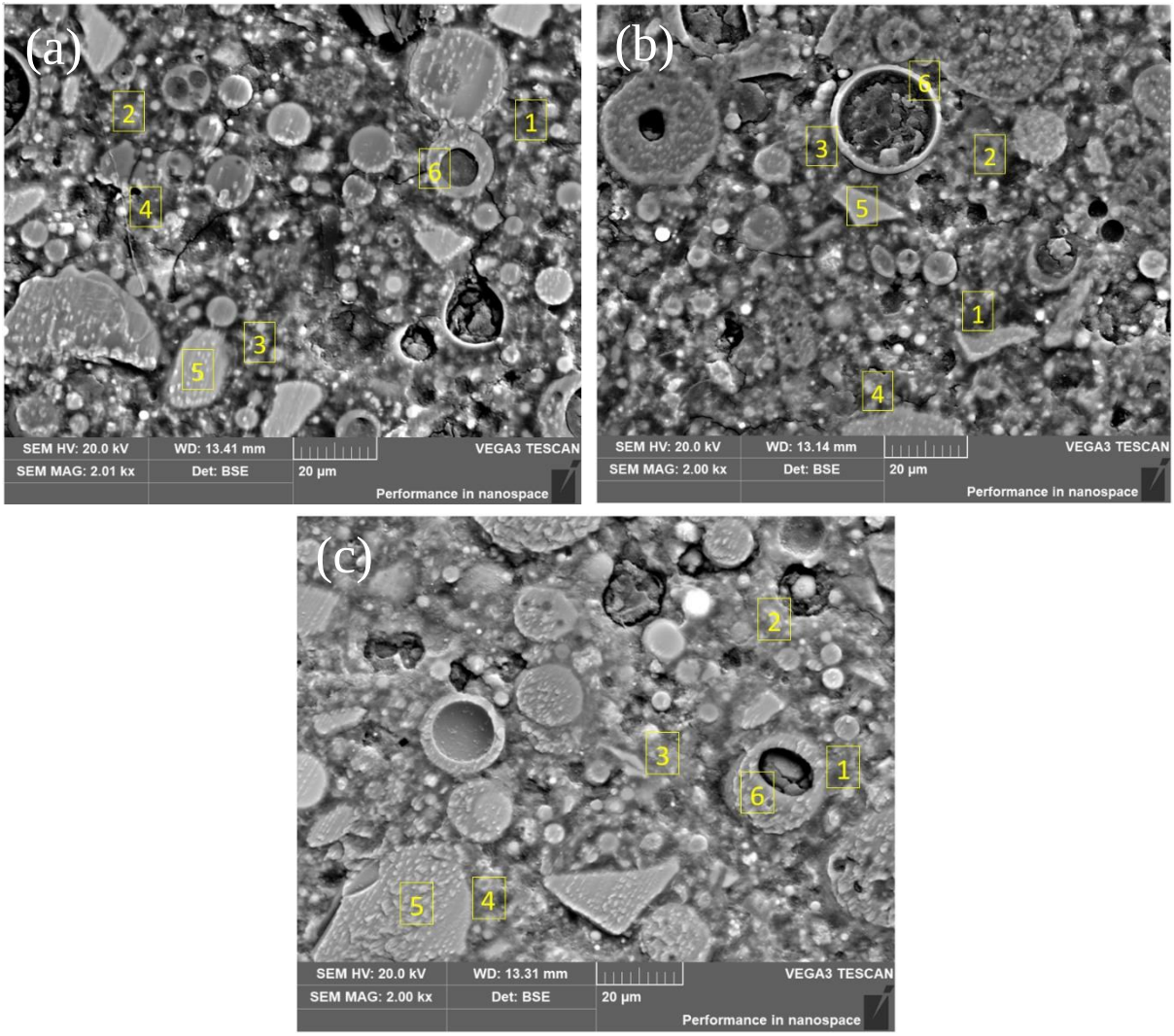

Fig. 6. SEM-BSE images of AAMs (a) FGR-0.24; (b) FGR-0.32 and (c) FGR-0.40

Table 3. EDS points analysis and corresponding reaction products

Area	Mix ID	Na	Al	Si	Ca	Si/Al	Ca/Si	Description
1	FGR-0.24	8.88	33.10	44.60	4.81	1.35	0.11	N-A-S-H
2		6.69	18.35	38.31	20.48	2.09	0.53	C-A-S-H
3		12.83	22.79	34.81	9.62	1.53	0.28	N-(C)-A-S-H
4		10.32	20.42	45.56	14.11	2.23	0.31	C-(N)-A-S-H
5		1.13	23.15	31.50	34.74	1.36	1.10	Slag
6		0.84	54.14	38.93	2.23	0.72	0.06	Reacted FA
1	FGR-0.32	15.35	24.57	35.09	8.95	1.43	0.26	N-A-S-H
2		7.56	16.73	36.02	25.17	2.15	0.70	C-A-S-H
3		15.09	22.2	38.99	10.75	1.76	0.28	N-(C)-A-S-H
4		10.25	20.95	41.15	13.04	1.96	0.32	C-(N)-A-S-H
5		0.51	15.86	33.12	41.63	2.09	1.26	Slag
6		1.6	77	14.93	3.51	0.19	0.24	Reacted FA
1	FGR-0.40	14.39	24.88	41.08	6.81	1.65	0.17	N-A-S-H
2		5.11	20.72	31.55	26.06	1.52	0.83	C-A-S-H
3		13	27.99	34.93	9.98	1.25	0.29	N-(C)-A-S-H
4		10.42	25.24	33.02	14.16	1.31	0.43	C-(N)-A-S-H
5		0.7	21.67	30.94	36.42	1.43	1.18	Slag
6		3.44	46.51	41.55	1.13	0.89	0.03	Reacted FA

Raw FA	1.75	0.24	Raw FA
Raw Slag	1.96	1.99	Raw Slag

The elemental ratios (Na/Si vs Ca/Si and Si/Al vs Na/Al) for the AAMs are shown in Fig. 7a and Fig. 7b. These plots were further analyzed statistically to understand the influence of element ratios on the reaction products of AAMs. Dispersion and central tendency of different ratios were evaluated by descriptive statistical analysis. The difference between the atomic ratios of different AAMs was determined with a confidence interval of 95% by ANOVA as shown in Table 4. Based on the results, grouping of elemental ratios was done by Tukey test to show if there was a significant difference between the two elemental ratios of two AAMs (i.e. same letter for an atomic ratio of two AAMs means no significant difference between two AAMs) (Mathews, 2005). The atomic ratios of AAMs show wide dispersion and overlapping. Some data points could be unusual where minimum and maximum ratios can be very far from the mean, 1st quartile and 3rd quartile values.

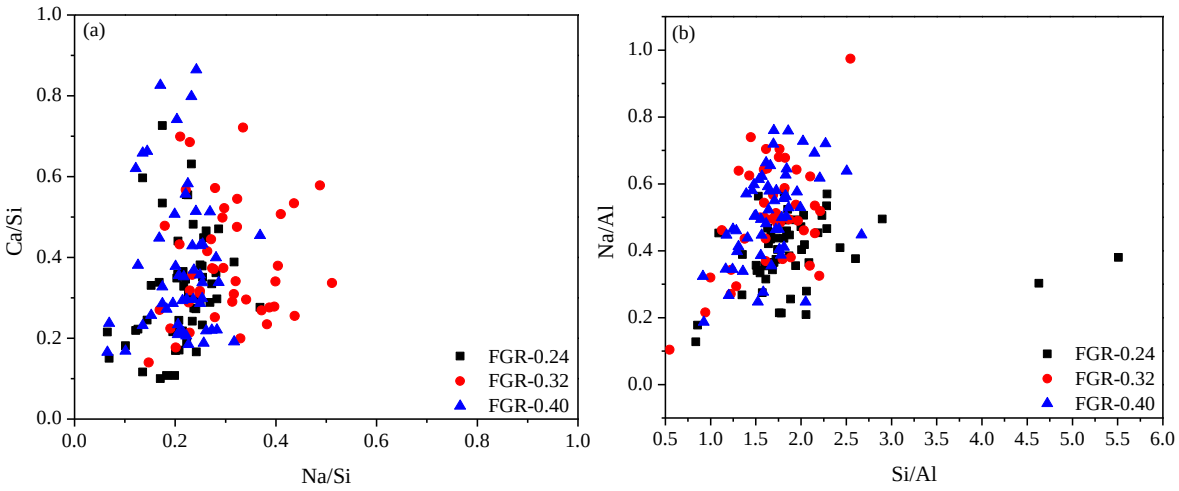

Fig. 7. Plots for elemental ratios of AAMs (a) Na/Si vs Ca/Si and (b) Si/Al vs Na/Al

There was no statistically significant difference observed for the Ca/Si among the different AAMs when amount of FGR was increased from 24% to 40% as all the AAMs fall in same group A. For the FGR-0.24, Ca/Si values were mostly clustered between 0.10 and 0.38 (3rd quartile), which was in between 0.14 to 0.50 and 0.17 to 0.46 for FGR-0.32 and FGR-0.40 respectively. It shows that a slightly higher amount of Ca based products (C-A-S-H) were formed in FGR-0.32 and FGR-0.40. It is worth noting that Ca/Si, Na/Si, Si/Al and Na/Al ratios for the FGR-0.32 and FGR-0.40 fall in similar groups A, A, B

and A respectively. This confirms that the chemical composition of these two mixtures was closer to each other. FGR-0.24 shows different grouping for the Na/Si, Si/Al and Na/Al ratios, hence its chemical composition is considered to be significantly different from FGR-0.32 and FGR-0.40. The higher ratio of Ca/Si, Na/Si, Na/Al, in FGR-0.32 and FGR-0.40 as compared to FGR-0.24 indicates that the incorporation of Na^{+} and Ca^{2+} into reaction products was increased with the increase in content of FGR. This means that the reactivity of slag (which is a major source of Ca^{2+}) was increased with the content of FGR. The increase in Na^{+} content is expected as it was major element present in chemical composition of FGR. The lower Si/Al ratio of FGR0-0.32 and FGR-0.40 indicates that higher amount of Al^{3+} was incorporated in reaction products and therefore increases the reaction degree of FA.

Table 4. Statistical analysis of SEM-EDS point analysis and grouping of different atomic ratios

Element Ratio	Sample ID	Mean	Min	1st quartile	Median	3rd quartile	Max	Tukey Test	
Ca/Si	FGR-0.24	0.32	0.10	0.22	0.30	0.38	0.73	A	
	FGR0.32	0.38	0.14	0.28	0.34	0.50	0.72	A	
	FGR-0.40	0.37	0.17	0.23	0.35	0.46	0.86	A	
Na/Si	FGR-0.24	0.21	0.07	0.17	0.22	0.25	0.37		B
	FGR0.32	0.30	0.15	0.23	0.29	0.37	0.51	A	
	FGR-0.40	0.31	0.12	0.27	0.31	0.36	0.45	A	
Si/Al	FGR-0.24	1.94	0.84	1.63	1.81	2.06	5.51	A	
	FGR0.32	1.65	0.38	1.43	1.69	1.94	2.55		B
	FGR-0.40	1.66	0.91	1.47	1.66	1.83	2.67		B
Na/Al	FGR-0.24	0.40	0.13	0.34	0.40	0.47	0.57		B
	FGR0.32	0.49	0.07	0.37	0.50	0.62	0.97	A	
	FGR-0.40	0.51	0.19	0.41	0.50	0.60	0.76	A	

3.5 Micromechanical Properties of FGR-AAMs

The micromechanical properties of AAMs were determined by nanoindentation test on the reaction products. Different reaction products (N-A-S-H, C-A-S-H and C-N-A-S-H gels) of AAMs can be quantified based on their hardness and elastic modulus values. The sites chosen for indentation were mainly gel pastes (reaction products) while unreacted phases (e.g., unreacted FA or slag particles) were avoided. The surface roughness of polished samples was captured by the scanning probe microscopy (SPM) as shown in Fig. 8. The surface roughness values for the FGR-0.24, FGR-0.32 and FGR-0.40 were 169.1 nm, 183.4 nm and 123 nm respectively.

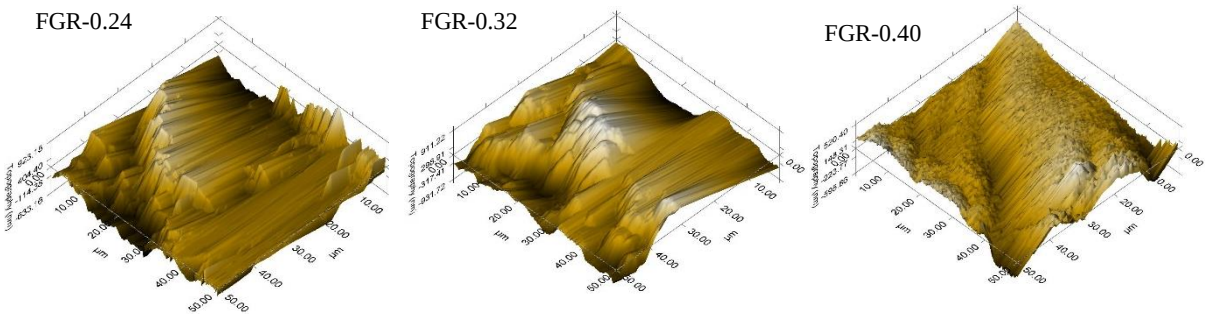

Fig. 8. Topography of polished AAMs pastes measured by SPM imaging technique

The micromechanical properties (elastic modulus) of AAMs are presented in the form of contour maps in Fig. 9. Normally, the elastic modulus of slag particles falls between 40-75 GPa (Hosseini et al., 2021; Nedeljković et al., 2018), whereas FA and Fe particles have elastic modulus higher than 75 MPa. The elastic modulus of pores is lower and lies between 0.1-1.0 GPa (Fang and Zhang, 2020; Ma et al., 2017). The elastic modulus of reaction products is lower than the unreacted particles and higher than the pores. The elastic modulus of reaction products in AAMs follows as C-A-S-H > N-C-A-S-H > N-A-S-H (Fang et al., 2021). It can be observed from the contour map of FGR-0.24 paste that its microstructure was significantly different from those of FGR-0.32 and FGR-0.40. The reaction products majorly consisted of geopolymer gel (N-A-S-H) as the elastic modulus fell under 20 GPa and a lower amount of cross-linked gel (N-C-A-S-H) was present. However, when amount of FGR was increased from 24% to 32%, the nature of reaction products was changed as the elastic modulus of reaction products was higher than those of FGR-0.24. The majority of reaction products in FGR-0.32 consisted of N-A-S-H gel and cross-linked gel N-C-A-S-H (E ≅ 20-30 GPa). A lower amount of C-A-S-H gel (E ≅ 30-40 GPa) was present in FGR-0.32. With the further increase in amount of FGR to 40%, formation of C-A-S-H gel was further increased. However, it is worth mentioning that volume of unreacted particles (E > 40 GPa) was significantly higher in FGR-0.40 pastes. It means that higher quantities of FGR could result in a weak cementing effect separating the different reaction products.

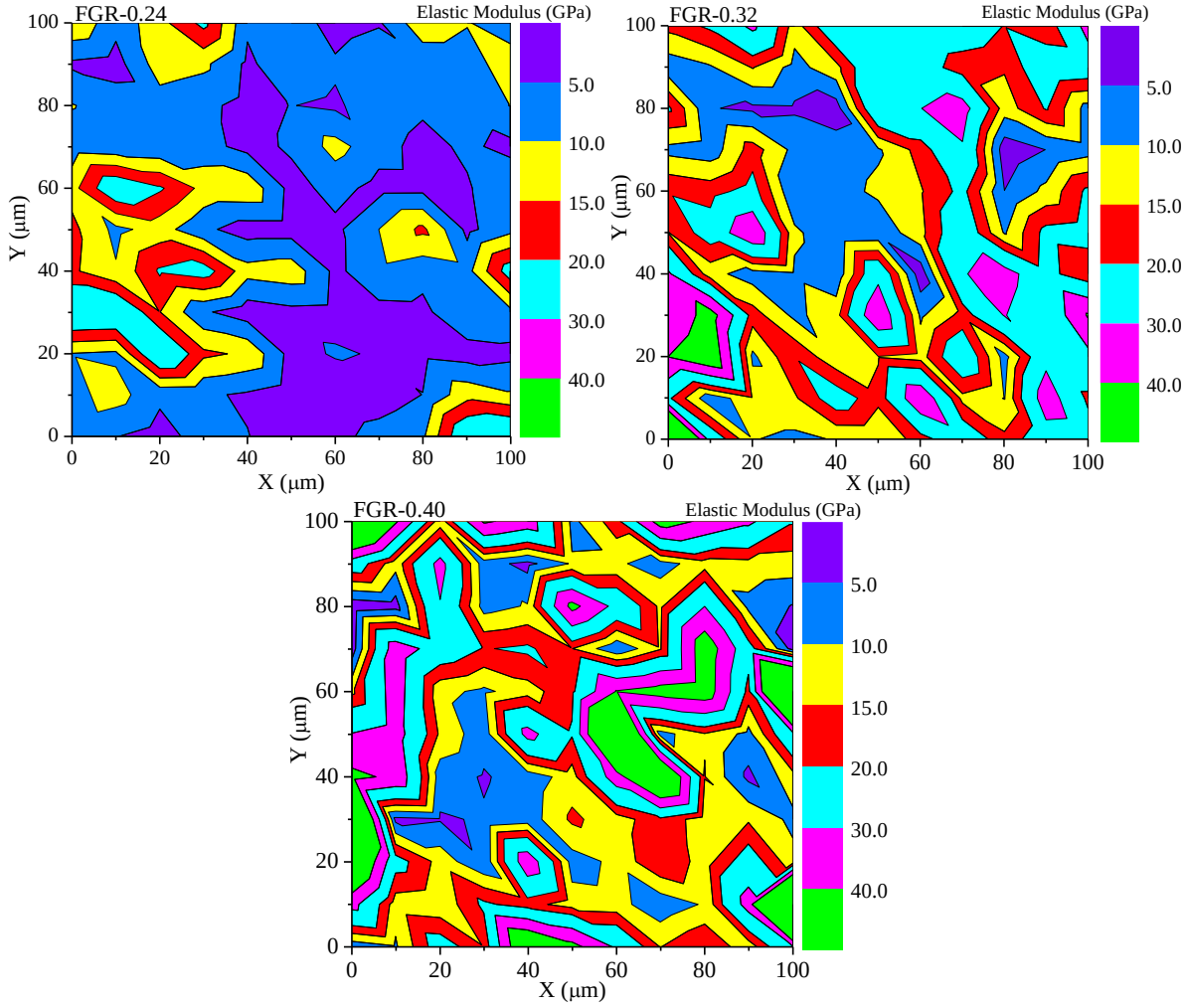

Fig. 9. Elastic modulus contour map of AAMs activated by FGR

The cluster allocation for the different reaction products of AAMs are shown by the elastic modulus (E) vs hardness (H) plots in Fig. 10. Elastic modulus and hardness of AAMs can be related to their stiffness and strength respectively. The clusters of nanoindentation data were characterized for the mechanical properties using the Gaussian deconvolution method. The process involves fitting experimental data, identification of different phases and quantification of data. The first step was to fit the frequency density vs elastic modulus histograms by the Gaussian distribution function. Four gaussian distribution curves were considered which include three reaction products (N-A-S-H, N-C-A-S-H and C-A-S-H gels) and unreacted phases (Fang et al., 2021). The area of curves was calculated to determine the volume of different phases as given in table 5.

Reaction products (gels) can be present in different states based on their elastic modulus (Luo et al., 2020). Depending on the elastic modulus, major reaction product was N-A-S-H gel (91.05%) in the FGR-0.24 paste along with the N-C-A-S-H gel (8.95%). N-A-S-H gel was further categorized into low density (LD), medium density (MD) and high density (HD) based on the elastic modulus. The strength of LD gel is lower as compared to the MD and HD gels as seen from their corresponding hardness values. Moreover, LD gel (E ≅ 3-6 GPa) was present in a higher volume as compared to MD gel ((E ≅ 6-10 GPa)), while a very low volume of HD gel (E ≅ 10-18 GPa) was present. With the increase in amount of FGR from 24% to 32%, the microstructure of FGR-0.32 was significantly changed as multiple types of gels were present in the paste. According to elastic modulus, reaction products of FGR-0.32 comprised N-A-S-H gel (62.8%), N-C-A-S-H gel (32.34%) and C-A-S-H gel (4.86%). The volume of LD and MD N-A-S-H gels was reduced whereas the volume of HD N-A-S-H gel was increased to a higher extent. It is also worth noting that the strength of HD N-A-S-H gel in FGR-0.32 was also higher than that of FGR-0.24. Besides, a significant amount of cross-linked gel was formed in FGR-0.32 which was present in lower quantities in FGR-0.24. C-A-S-H gel was also present in a low amount of 4.86%. Some unreacted particles were also detected. It can be observed that strength of cross-linked gel was greater than that of N-A-S-H gel but slightly lower than that of C-A-S-H gel. When amount of FGR was increased to 40%, volume of cross-linked N-C-A-S-H gel was decreased to 20.4% whereas volume of C-A-S-H gel was increased to 17.5% as compared to FGR-0.32. There were no changes in the formation of N-A-S-H gel amount when FGR amount was increased from 32% to 40%. However, the volume of unreacted phases was slightly higher in FGR-0.40, which could have a negative impact on the mechanical performance of FGR-0.4.

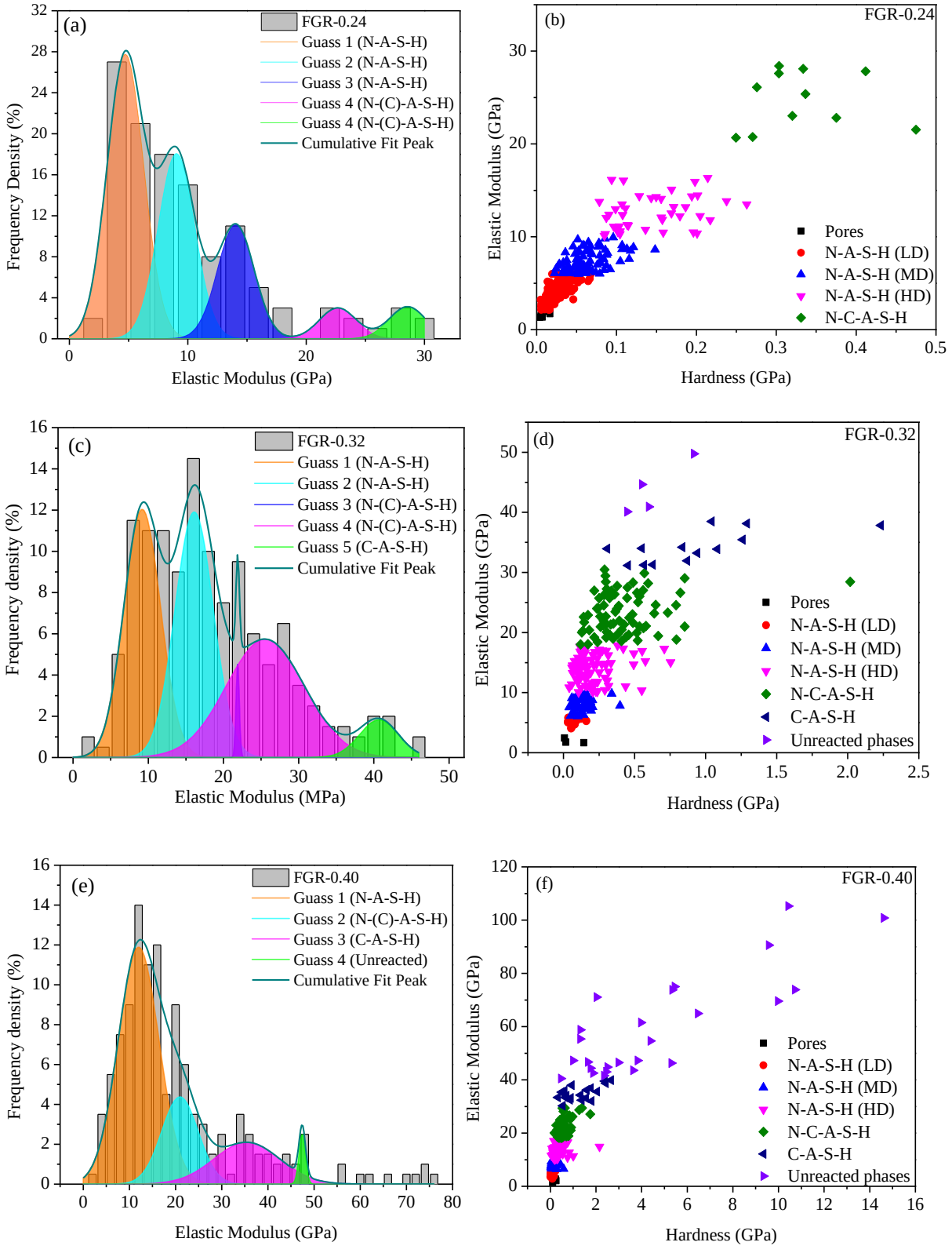

Fig. 10. Gaussian deconvolution of histograms of Elastic modulus of AAMs (a, c and e) and Hardness vs Elastic Modulus plots (b, d and f) respectively

Table 5. Composition of gel phases in AAMs activated by FGR

Reaction product	FGR-0.24	FGR-0.32	FGR-0.40
N-A-S-H	91.05	62.8	62.1
N-C-A-S-H	8.95	32.34	20.4
C-A-S-H	0	4.86	17.5
Unreacted phases	0	0	1.99

3.6 Compressive Strength of FGR-AAMs

The influence of FGR on the performance of compressive strength of AAMs is plotted in Fig. 11. The compressive strength of FGR-0.24 was 33.5 MPa. For the pastes containing 32% FGR, the compressive strength was increased to 39.6 MPa, which was 18.41% higher than that of FGR-0.24. However, with the further increase in FGR to 40%, there was a decline in strength (8.58%) to 35.5 MPa as compared to FGR-0.32. This indicates that the optimum proportion of FGR to prepare AAM is about 32%. The results of SEM corroborate the compressive strength results as reaction products consisted of higher average Ca/Si ratio in FGR-0.32 as compared to FGR-0.24 indicating the formation of products incorporating higher amounts of Ca^{2+} (C-A-S-H, C-N-A-S-H). Similarly, nanoindentation results proved that higher amount of cross-linked gel (C-N-A-S-H) and C-A-S-H gel was present in FGR-0.32. These gels have higher strength than that of N-A-S-H and consequently improved the strength of pastes. According to SEM results, chemical composition of reaction products of FGR-0.32 and FGR-0.40 was similar, however, volume of unreacted phases was slightly increased in FGR-0.40 according to nanoindentation results. Although a higher amount of FGR (Na_2SO_4) increased the amount of Ca-rich C-A-S-H gel, the filler effect of Na_2SO_4 in FGR-0.40 was more dominant and the strength was slightly decreased as compared to FGR-0.32. The results of compressive strength of FGR-AAMs are compared with the waste derived based activators AAMs reported in literature in Table 6. It can be observed that FGR based activator showed higher compressive strength as compared to the AAMs prepared from solidified waste cleaning agent (SWCA) and biomass ashes (BA) based waste-derived activators. The results of AAMs incorporating coffee husk ash (CHA) are in similar range as the FGR-AAMs. However, it is important to mention that precursors used in literature is based on solely granulate blast furnace slag (GBFS), which is relatively expensive and has significantly higher reactivity as compared

to FA. Moreover, chemical composition of activators and activator to precursors ratio also influence the reaction mechanism to great extent.

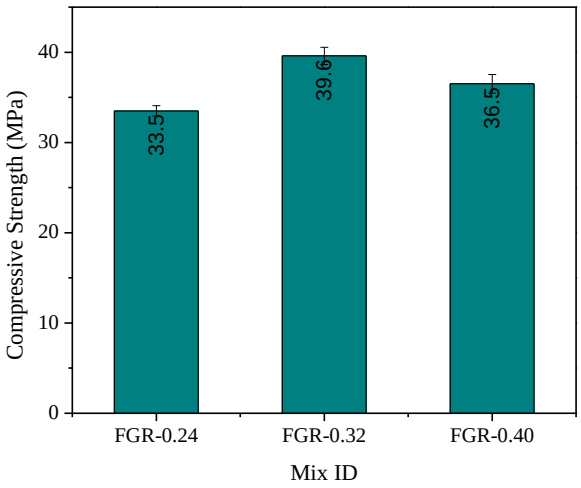

Fig. 11. Compressive strength of AAMs

Table 6. Compressive strength comparison of FGR-AAMs and waste derived activator based AAMs

Reference	Mix ID	Waster Activator	Chemical Composition	Precursors	Activator/ precursor	28-d Compressive strength (MPa)
This study	FGR-0.24	FGR	Na_2O (38.3%) SO_4 (31.9%)	FA and slag	0.24	33.5
	FGR-0.32				0.32	39.5
	FGR-0.40				0.40	36.5
(Fořt et al., 2022)	GWA24	SWCA*	NaOH (95%)	Slag	0.24	25.0
	GWA32				0.32	22.0
	GWA40				0.40	19.0
	GWA48				0.48	18.0
	GWA56				0.56	20.0
(Soriano et al., 2022)	NBA-0.33	NBA	K_2O (37.3%) CaO (34.01)	Slag	0.33	25.05
	MBA-0.33	MBA	K_2O (38.2%) CaO (8.26%)		0.33	26.85
	HBA-0.33	HBA	K_2O (31.81%) CaO (30.02%)		0.33	27.21
(Lima et al., 2023)	CHA-5 %	CHA	K_2CO_3 (100%)	Slag	.05	21.6
	CHA-10 %				0.10	30.0
	CHA-15 %				0.15	35.9
	CHA-20 %				0.20	39.8
	CHA-25 %				0.25	40.9

*Abbreviations: FGR: Flue gas residue, SWCA: Solidified waste cleaning agent, NBA: Nutshell biomass ash, MBA: Mango biomass ash, HBA: hazelnut shell ashes, CHA: Coffee husk ash

3.7 Microstructure study of FGR-AAMs

Fig. 12 shows the micro-XCT representation of AAMs with different FGR contents. The porosity of FGR-0.24 was 1.88%. For the pastes containing 32% FGR, the porosity decreased to 1.23%, which was

34.5% less than that of FGR-0.24. With the further increase in FGR to 40%, there was a further decline in porosity (37.7%) to 1.17%, compared to FGR-0.24. It is worth noting that increasing the amount of FGR decreases the porosity and maximum pore diameter of AAMs. The decrease in porosity is due to the formation of products incorporating higher amounts of Ca^{2+} (C-A-S-H, C-N-A-S-H) in FGR-0.32 as compared to FGR-0.24, as discussed in SEM and nano-indentation results. However, the porosity of FGR-0.32 (1.23%) and FGR-0.40 (1.17%) showed marginal difference. SEM also found that the chemical composition of reaction products of FGR-0.32 and FGR-0.40 was similar; however, the volume of unreacted phases was slightly increased in FGR-0.40 as indicated in nanoindentation results. As particle size of FGR (7µm) is significantly lower than that of FA (20.1µm) and slag (14.1µm), the filler effect of FGR at higher content level (in FGR-0.40) could result in decreased porosity and pore diameter compared to FGR-0.24 and FGR-0.32.

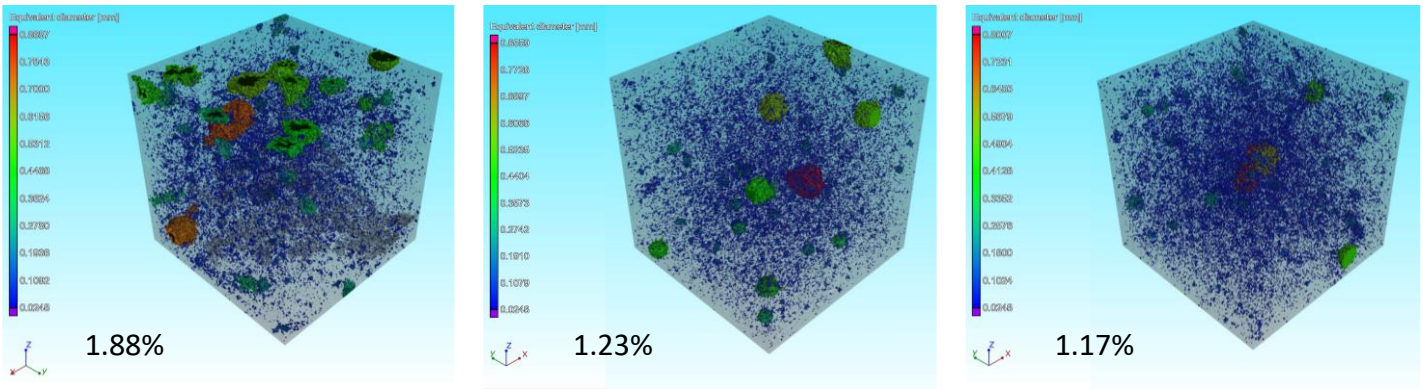

FGR-0.24 FGR-0.32 FGR-0.40

Fig. 12. XCT of FGR-AAMs

3.8 Heavy metal leaching

The total concentration of heavy metals present in FGR is plotted in Fig. 13a. FGR consisted of several heavy metals including Zn, Cu, Ba, Cr, As, Pb, Ni, Ag and Cd in descending order. The total concentration of Zn was 1019 mg/L whereas Cu, Ba, Cr and As were present in 266, 173, 100 and 76 mg/L concentrations respectively. Other heavy metals were present in lower amounts. According to the total concentration results of FGR, heavy metals were present in considerably high amounts and toxicity of FGR should be checked. The toxicity of waste material is linked to the soluble concentration of heavy metals which was tested by the TCLP and SPLP tests. The results of soluble concentration of heavy

metals determined from TCLP and SPLP tests for FGR are shown in Fig. 13b. The leaching concentrations of all heavy metals were far below the regulatory limits fixed by U.S. EPA standard as shown in Table 7. Hence, FGR could be classified as a non-hazardous material and could be utilized safely in recycling for construction material practices.

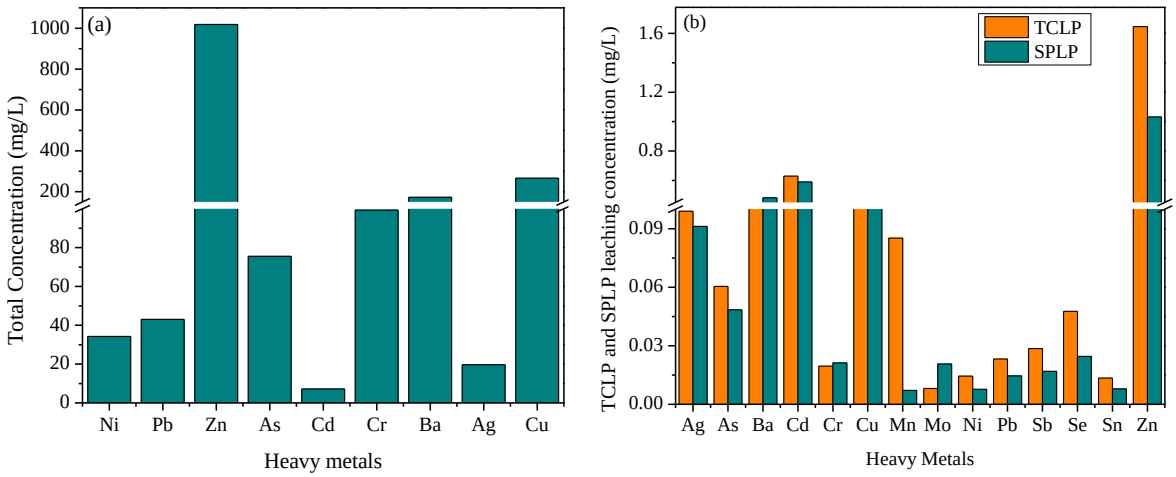

Fig. 13. (a) The concentration of heavy metals in APCr and (b) Leaching concentration determined by TCLP and SPLP methods

Table 7. Leaching concentration of heavy metals (mg/L)

Heavy metals	Ag	As	Ba	Cd	Cr	Cu	Mn	Mo	Ni	Pb	Sb	Se	Sn	Zn
TCLP leaching	0.10	0.06	0.40	0.63	0.02	0.26	0.09	0.01	0.01	0.02	0.03	0.05	0.01	1.65
SPLP leaching	0.09	0.05	0.48	0.59	0.02	0.22	0.01	0.02	0.01	0.01	0.02	0.02	0.01	1.03
U.S. EPA max. limits	5.0	5.0	100	1.0	5.0	-	-	-	-	5.0	-	1.0	-	100

4 Discussion

FGR as an industrial waste from an incineration plant is utilized to source the alkaline-activator (Na_2SO_4) for the activation of high-volume fly ash and slag cement paste. Alkali-silicate based activators commonly used to produce AAMs are energy intensive, expensive and contribute to a higher amount of carbon emission (60-70%) for AAMs. Utilizing FGR residue will not only solve the problem of landfill disposal of waste materials but also significantly cut down the production cost and carbon emission of AAMs. AAM pastes were prepared by mixing the fixed ratio of slag (30%) and fly ash (70%) precursors with varying ratios of FGR to precursors of 24%, 32% and 40%. Based on the results, the synergistic effect of FGR on the properties of FA and slag-based AAMs is discussed below.

556 The major band of reaction products in AAMs is located around 987-988 cm^{-1} and shifted from its
557 original positions in precursors due to the formation of reaction products. The range of characteristic
558 bands for all pastes is lower than the characteristic band of N-A-S-H gel (1030 cm^{-1}) and higher than
559 that of C-A-S-H gel (940 cm^{-1}), which confirms that multiple gel reaction products might be present in
560 geopolymer pastes (Zhang et al., 2017). Another band from FTIR analysis around 1100 cm^{-1} is linked
561 to the anti-symmetric stretching vibration SO_4^{2-} bond. The SO_4^{2-} can replace the tetrahedral silica (SiO_4)
562 in reaction products (e.g N-A-S-H) which (SiO_4) in a free state can further accelerate the active alumina
563 dissolution. Hence, an increase in FGR inspires the formation of new Al-O-Si and Si-O-Si bonds in
564 FGR added AAM system and a new glassy Si-O-Si (Al) phase is formed to enhance the reaction degree
565 of AAM materials (Li et al., 2012). However, the addition of FGR over a certain limit can retard the
566 reaction degree as increase rate of SO_4^{2-} is much faster as compared to the dissolution rate of precursors
567 (aluminosilicates) which can be observed by the sharp peak at 1102 cm^{-1}. It could lead to increase in
568 unreacted precursors and reduce the volume of reaction products which in turn will also reduce the
569 mechanical properties of AAMs (Lv et al., 2020). It is postulated that an additional C-A-S-H gel or
570 cross-linked gel (N-C-A-S-H) was formed in AAM pastes containing a higher percentage of FGR
571 (FGR-0.32) as compared to FGR-0.24. Some studies on the zeolite-based materials have also reported
572 that a peak around 1100 cm^{-1} is linked to in-plane hydroxyl bending modes of Si-O-Al in the triangular
573 form (Jacobs et al., 1994). Moreover, hybrid pastes containing FA and slag result in multiple gel
574 products (C-A-S-H, N-A-S-H and cross-linked C-N-A-S-H gel) (Aiken et al., 2018).

575 XRD results revealed that the dissolution of Na_2SO_4 is higher at a lower amount of FGR (24%),
576 however, when the addition of FGR is above the optimum limit of 32%, its dissolution is reduced. The
577 major reaction product in all AAM pastes is considered to be N-A-S-H gel which can be identified
578 through a shifted broad hump (20-40° 2θ) (Lv et al., 2020; Moutaoukil et al., 2022; Wang et al., 2022)
579 along with the presence of C-(A)-S-H, zeolite, berlinite and apatite phases. The XRD patterns of all
580 pastes show reaction products of disordered nature, which is consistent with the reaction products in
581 AAMs (Wang et al., 2022). According to TGA results, the volume of major reaction products N-A-S-
582 H/C-A-S-H differed slightly among different AAM pastes. However, it indicated that unreacted amount

583 of salt (Na_2SO_4) increased with the increase in percentage of FGR (Amutha Rani et al., 2008; Bogush
584 et al., 2019). This finding validated the XRD results.

585 SEM-EDS results suggested the formation of multiple gels including N-A-S-H, N-C-A-S-H and C-A-
586 S-H. The formation of multiple gels has been reported in the literature in hybrid AAMs containing
587 aluminosilicate (FA or metakaolin) and calcium (slag or limestone) precursors (Mills et al., 2022; Perez-
588 Cortes and Escalante-Garcia, 2020; Rafeet et al., 2019; S. Zhang et al., 2021). The quantification of
589 reaction products is difficult by the SEM-EDS as these phases are highly intermixed on a very small
590 scale and difficult to resolve by SEM-EDS. Therefore, results from each EDS point analysis possibly
591 represent the chemical composition of at least two kinds of phases interacting with the electron beam.
592 Consequently, nanoindentation technique was further used to quantify the reaction products of AAMs.
593 The nanoindentation results validated the SEM results as an increase in amount of FGR residue
594 increased the volume of C-A-S-H. The strength (hardness value) of reaction products was also
595 significantly improved with the increase in FGR amount. The higher percentage of FGR (Na_2SO_4) at
596 40% promoted the formation of C-A-S-H gel, however, the volume of N-A-S-H gel was not changed
597 above 32%. The formation of higher volume of C-A-S-H for AAMs containing higher content of FGR
598 is linked to the acceleration of slag dissolution (leaching out of more Ca^{2+}) in liquid phase (Zhang et
599 al., 2021). The use of Na_2SO_4 in cementitious materials is reported to increase the pH value of pastes
600 due to formation of NaOH and accelerate the dissolution of Ca^{+2}, Si^{+4} and Al^{+3} which participate to
601 form reaction products (C-A-S-H, N-A-S-H), hence improving the compactness of microstructure and
602 mechanical properties of cement pastes (Zhang et al., 2021). However, compressive strength declined
603 at a relatively higher FGR content of 40% as higher volume of unreacted phases was observed from
604 nanoindentation. This decrease in strength was due to the fact that excess Na_2SO_4 did not participate in
605 the reaction and migrated toward the surface of paste. Finally, heavy metal leaching results from TCLP
606 and SPLP methods showed that FGR was safe to be utilized as an alkaline activator in the construction
607 industry without any concerns of heavy metal leaching.

5 Carbon emission assessment of FGR-based AAMs

Besides being the most expensive component, commercially produced alkali hydroxide and alkali silicate-based activators also contribute to considerably higher carbon emissions ranging from 40-80% of AAMs as per literature (Bajpai et al., 2020; Bernal et al., 2016; Habert et al., 2011; Passuello et al., 2017). The emission of carbon from the production of slag and FA per metric ton is estimated to be 79 kg and 27 kg respectively. For the NaOH and water glass-based activators, these emission values correspond to 1915 kg and 1514 kg per metric ton respectively (Turner and Collins, 2013). The carbon emission from FGR based AAMs are mainly associated with the grinding of FGR in ball mill for 4 hours and heat curing of AAMs. However, the positive impact of using industrial waste FGR as an alternative source of costly and energy intensive commercial alkaline activators (produced by heating sodium bicarbonate and silica at 1200-1400℃) is significant in terms of its negligible carbon emission and cost (Fawer et al., 1999). Using FGR to produce AAMs can offer several advantages, including: (1) increased recycling of FGR industrial waste, which can help achieve carbon neutrality goals in waste management, (2) decreased waste disposal burdens on landfills, and reduced potential environmental risks associated with heavy metal leaching, and (3) lowered production costs and carbon emissions of AAMs by utilizing FGR as an alternative to expensive and energy-intensive commercial activators.

6 Conclusions

FGR is an industrial alkaline waste produced from the incineration of sewage sludge at the WtE plants and collected at the downstream after flue gas treatment process. In this study, FGR was used as a source of alkaline activator due to the presence of high content of Na_2SO_4. AAM pastes were produced by mixing the FA, slag and FGR. Heat curing scheme was adopted due to the low reactivity of FGR at an ambient temperature. Reaction products of AAMs were characterized through advanced analysis techniques including FTIR, XRD, TGA, SEM and nanoindentation.

1. The FTIR results indicated that incorporating FGR led to the formation of multiple reaction products or hybrid gel. The main band (at 988 cm^{-1}) of the reaction products was observed to exist between the main bands of N-A-S-H gel and C-A-S-H gel. Additionally, the presence of

SO_4^{2-} ions was found to accelerate the dissolution of alumina and enhance the reaction degree of precursors.

2. The presence of a wide peak within the 20-40° 2θ range indicates that the reaction products in AAMs are amorphous in nature. Additionally, several new phases were formed during the reaction process, including zeolite, calcite, apatite, and berlinite.
3. The TGA results demonstrate that AAMs exhibit a more pronounced weight loss in the temperature range of 0-300°C, which can be attributed to the dehydroxylation of the N-A-S-H gel. Conversely, the range of 300-600°C is associated with the removal of water from the C-A-S-H gel, leading to a lesser degree of mass loss. These observations suggest that N-A-S-H gel is the primary reaction product in all AAMs, instead of C-A-S-H gel.
4. EDS analysis validated the presence of N-A-S-H, C-A-S-H, and N-C-A-S-H gels in the reaction products of AAMs. The amount of C-A-S-H gel was found to be positively correlated with the FGR content. Additionally, a statistical analysis of the SEM-EDS data revealed that the chemical composition of the FGR-0.32 and FGR-0.40 samples were significantly similar to each other.
5. FGR-0.24 mainly consisted of N-A-S-H gel, which accounted for 91.05% of the reaction products. However, an increase in the amount of FGR to 32% and 40% changed the micromechanical properties and reaction products. Higher amount of Ca^{2+} was incorporated into reaction products indicating that higher content of Na_2SO_4 could increase the reactivity of slag. Nonetheless, it should be noted that the volume of unreacted phases was found to increase when the FGR content exceeded the optimal threshold of 32%. This factor could lead to a reduction in mechanical performance.
6. The compressive strength of FGR-0.32 paste was higher as compared to FGR-0.24 due to enhanced activation of slag at higher FGR content. However, filler effect of FGR was dominant for high contents of 40% and strength of FGR-0.40 was slightly reduced. TCLP and SPLP methods showed that FGR may be used as a safe construction material without any concerns about heavy metal leaching.

7. The improvement in mechanical and microstructural performance of AAMs is expected upon introducing the amorphous silica source along with FGR and should be studied further in the future.

References:

Ahmad, M.R., Lao, J., Dai, J.-G., Xuan, D., Poon, C.S., 2022. Upcycling of air pollution control residue waste into cementitious product through geopolymerization technology. Resour Conserv Recycl 181, 106231. https://doi.org/10.1016/J.RESCONREC.2022.106231

Ahmad, M.R., Qian, L.P., Fang, Y., Wang, A., Dai, J.G., 2023. A multiscale study on gel composition of hybrid alkali-activated materials partially utilizing air pollution control residue as an activator. Cem Concr Compos 136, 104856. https://doi.org/10.1016/J.CEMCONCOMP.2022.104856

Aiken, T.A., Kwasny, J., Sha, W., Soutsos, M.N., 2018. Effect of slag content and activator dosage on the resistance of fly ash geopolymer binders to sulfuric acid attack. Cem Concr Res 111, 23–40. https://doi.org/10.1016/J.CEMCONRES.2018.06.011

Alnahhal, M.F., Hamdan, A., Hajimohammadi, A., Kim, T., 2021. Effect of rice husk ash-derived activator on the structural build-up of alkali activated materials. Cem Concr Res 150, 106590. https://doi.org/https://doi.org/10.1016/j.cemconres.2021.106590

Amutha Rani, D., Gomez, E., Boccaccini, A.R., Hao, L., Deegan, D., Cheeseman, C.R., 2008. Plasma treatment of air pollution control residues. Waste Management 28, 1254–1262. https://doi.org/https://doi.org/10.1016/j.wasman.2007.06.008

Bajpai, R., Choudhary, K., Srivastava, A., Sangwan, K.S., Singh, M., 2020. Environmental impact assessment of fly ash and silica fume based geopolymer concrete. J Clean Prod 254, 120147. https://doi.org/https://doi.org/10.1016/j.jclepro.2020.120147

Bernal, S.A., Provis, J.L., Walkley, B., San Nicolas, R., Gehman, J.D., Brice, D.G., Kilcullen, A.R., Duxson, P., van Deventer, J.S.J., 2013. Gel nanostructure in alkali-activated binders based on slag and fly ash, and effects of accelerated carbonation. Cem Concr Res 53, 127–144. https://doi.org/https://doi.org/10.1016/j.cemconres.2013.06.007

Bernal, S.A., Rodríguez, E.D., Kirchheim, A.P., Provis, J.L., 2016. Management and valorisation of wastes through use in producing alkali-activated cement materials. Journal of Chemical Technology & Biotechnology 91, 2365–2388. https://doi.org/https://doi.org/10.1002/jctb.4927

Bogush, A., Stegemann, J.A., Wood, I., Roy, A., 2015. Element composition and mineralogical characterisation of air pollution control residue from UK energy-from-waste facilities. Waste Management 36, 119–129. https://doi.org/https://doi.org/10.1016/j.wasman.2014.11.017

Bogush, A.A., Stegemann, J.A., Roy, A., 2019. Changes in composition and lead speciation due to water washing of air pollution control residue from municipal waste incineration. J Hazard Mater 361, 187–199. https://doi.org/https://doi.org/10.1016/j.jhazmat.2018.08.051

Bogush, A.A., Stegemann, J.A., Zhou, Q., Wang, Z., Zhang, B., Zhang, T., Zhang, W., Wei, J., 2020. Co-processing of raw and washed air pollution control residues from energy-from-waste facilities in the cement kiln. J Clean Prod 254, 119924. https://doi.org/https://doi.org/10.1016/j.jclepro.2019.119924

Chen, W., Li, B., Wang, J., Thom, N., 2021. Effects of alkali dosage and silicate modulus on autogenous shrinkage of alkali-activated slag cement paste. Cem Concr Res 141, 106322. https://doi.org/https://doi.org/10.1016/j.cemconres.2020.106322

Das, G., Kakati, N., Lee, S.H., Karak, N., Yoon, Y.S., 2014. Water soluble sodium sulfate nanorods as a versatile template for the designing of copper sulfide nanotubes. J Nanosci Nanotechnol 14, 4455–4461.

di Bella, G., Arrigo, I., Catalfamo, P., Corigliano, F., Mavilia, L., 2003. Advances in the extraction of silica from glass cullet, in: Recycling and Reuse of Waste Materials. Thomas Telford Publishing, pp. 137–142.

EPD, E.P.D., 2021. Integrated Waste Management Facilities, Problems & Solutions [WWW Document]. URL https://www.epd.gov.hk/epd/english/environmentinhk/waste/prob_solutions/WFdev_IWMF.html

Fang, G., Wang, Q., Zhang, M., 2021. Micromechanical analysis of interfacial transition zone in alkali-activated fly ash-slag concrete. Cem Concr Compos 119, 103990. https://doi.org/https://doi.org/10.1016/j.cemconcomp.2021.103990

Fang, G., Zhang, M., 2020. Multiscale micromechanical analysis of alkali-activated fly ash-slag paste. Cem Concr Res 135, 106141. https://doi.org/https://doi.org/10.1016/j.cemconres.2020.106141

Fawer, M., Concannon, M., Rieber, W., 1999. Life cycle inventories for the production of sodium silicates. Int J Life Cycle Assess 4, 207. https://doi.org/10.1007/BF02979498

Fernández-Jiménez, A., Cristelo, N., Miranda, T., Palomo, Á., 2017. Sustainable alkali activated materials: Precursor and activator derived from industrial wastes. J Clean Prod 162, 1200–1209. https://doi.org/https://doi.org/10.1016/j.jclepro.2017.06.151

Fořt, J., Mildner, M., Keppert, M., Abed, M., Černý, R., 2022. Potential of industrial waste as alternative alkaline activator for development of eco-efficient mortars. Case Studies in Construction Materials e01716. https://doi.org/https://doi.org/10.1016/j.cscm.2022.e01716

García-Lodeiro, I., Fernández-Jiménez, A., Blanco, M.T., Palomo, A., 2008. FTIR study of the sol–gel synthesis of cementitious gels: C–S–H and N–A–S–H. J Solgel Sci Technol 45, 63–72.

Geraldo, R.H., Fernandes, L.F.R., Camarini, G., 2021. Mechanical properties of porcelain waste alkali-activated mortar. Open Ceramics 8, 100184. https://doi.org/https://doi.org/10.1016/j.oceram.2021.100184

Giergiczny, Z., 2019. Fly ash and slag. Cem Concr Res 124, 105826. https://doi.org/https://doi.org/10.1016/j.cemconres.2019.105826

Granizo, N., Palomo, A., Fernandez-Jiménez, A., 2014. Effect of temperature and alkaline concentration on metakaolin leaching kinetics. Ceram Int 40, 8975–8985. https://doi.org/10.1016/J.CERAMINT.2014.02.071

738 Habert, G., d'Espinose de Lacaillerie, J.B., Roussel, N., 2011. An environmental evaluation of
739 geopolymer based concrete production: reviewing current research trends. J Clean Prod 19,
740 1229–1238. https://doi.org/https://doi.org/10.1016/j.jclepro.2011.03.012

741 Hosseini, S., Brake, N.A., Nikookar, M., Günaydın-Şen, Ö., Snyder, H.A., 2021. Mechanochemically
742 activated bottom ash-fly ash geopolymer. Cem Concr Compos 118, 103976.
743 https://doi.org/https://doi.org/10.1016/j.cemconcomp.2021.103976

744 Hu, B., Zhao, S., Zhang, S., 2015. Removal of lead from cathode ray tube funnel glass by generating
745 the sodium silicate. J Air Waste Manage Assoc 65, 106–114.
746 https://doi.org/10.1080/10962247.2014.976721

747 Jacobs, W., van Wolput, J., van Santen, R.A., Jobic, H., 1994. A vibrational study of the OH and OD
748 bending modes of the Brönsted acid sites in zeolites. Zeolites 14, 117–125.

749 Keawthun, M., Krachodnok, S., Chaisena, A., 2014. Conversion of waste glasses into sodium silicate
750 solutions. International Journal of Chemical Sciences 12, 83–91.

751 Kourti, I., Rani, D.A., Deegan, D., Boccaccini, A.R., Cheeseman, C.R., 2010. Production of geopolymers
752 using glass produced from DC plasma treatment of air pollution control (APC) residues. J
753 Hazard Mater 176, 704–709. https://doi.org/https://doi.org/10.1016/j.jhazmat.2009.11.089

754 Kuri, J.C., Majhi, S., Sarker, P.K., Mukherjee, A., 2021. Microstructural and non-destructive
755 investigation of the effect of high temperature exposure on ground ferronickel slag blended fly
756 ash geopolymer mortars. Journal of Building Engineering 43, 103099.
757 https://doi.org/https://doi.org/10.1016/j.jobe.2021.103099

758 Lee, W.K.W., van Deventer, J.S.J., 2002. The effects of inorganic salt contamination on the strength
759 and durability of geopolymers. Colloids Surf A Physicochem Eng Asp 211, 115–126.
760 https://doi.org/https://doi.org/10.1016/S0927-7757(02)00239-X

761 Lei, L., Chan, H.-K., 2020. Investigation into the molecular design and plasticizing effectiveness of
762 HPEG-based polycarboxylate superplasticizers in alkali-activated slag. Cem Concr Res 136,
763 106150. https://doi.org/https://doi.org/10.1016/j.cemconres.2020.106150

764 Li, Q., Xu, H., Li, F., Li, P., Shen, L., Zhai, J., 2012. Synthesis of geopolymer composites from blends of
765 CFBC fly and bottom ashes. Fuel 97, 366–372.
766 https://doi.org/https://doi.org/10.1016/j.fuel.2012.02.059

767 Li, Z., Lu, T., Liang, X., Dong, H., Ye, G., 2020. Mechanisms of autogenous shrinkage of alkali-activated
768 slag and fly ash pastes. Cem Concr Res 135, 106107.
769 https://doi.org/https://doi.org/10.1016/j.cemconres.2020.106107

770 Lima, F.S., Gomes, T.C.F., Moraes, J.C.B., 2023. Effect of coffee husk ash as alkaline activator in one-
771 part alkali-activated binder. Constr Build Mater 362, 129799.
772 https://doi.org/https://doi.org/10.1016/j.conbuildmat.2022.129799

773 Lodeiro, I.G., Macphee, D.E., Palomo, A., Fernández-Jiménez, A., 2009. Effect of alkalis on fresh C–S–
774 H gels. FTIR analysis. Cem Concr Res 39, 147–153.

775 Luo, Z., Li, W., Gan, Y., Mendu, K., Shah, S.P., 2020. Applying grid nanoindentation and maximum
776 likelihood estimation for N-A-S-H gel in geopolymer paste: Investigation and discussion. Cem
777 Concr Res 135, 106112. https://doi.org/https://doi.org/10.1016/j.cemconres.2020.106112

778 Lv, Q., Wang, Z., Gu, L., Chen, Y., Shan, X., 2020. Effect of sodium sulfate on strength and
779 microstructure of alkali-activated fly ash based geopolymer. J Cent South Univ 27, 1691–1702.

780 Ma, Y., Ye, G., Hu, J., 2017. Micro-mechanical properties of alkali-activated fly ash evaluated by
781 nanoindentation. Constr Build Mater 147, 407–416.
782 https://doi.org/https://doi.org/10.1016/j.conbuildmat.2017.04.176

783 Maldonado-Alameda, A., Giro-Paloma, J., Rodríguez-Romero, A., Serret, J., Menargues, A., Andrés,
784 A., Chimenos, J.M., 2021. Environmental potential assessment of MSWI bottom ash-based
785 alkali-activated binders. J Hazard Mater 416, 125828.
786 https://doi.org/https://doi.org/10.1016/j.jhazmat.2021.125828

787 Mathews, P.G., 2005. Design of Experiments with MINITAB. ASQ Quality Press Milwaukee, WI, USA:

788 McLellan, B.C., Williams, R.P., Lay, J., van Riessen, A., Corder, G.D., 2011. Costs and carbon emissions
789 for geopolymer pastes in comparison to ordinary portland cement. J Clean Prod 19, 1080–1090.
790 https://doi.org/https://doi.org/10.1016/j.jclepro.2011.02.010

791 Method 1312, U.E., 1994. Synthetic Precipitation Leaching Procedure (SPLP).

792 Mills, J., Mondal, P., Wagner, N., 2022. Structure-property relationships and state behavior of alkali-
793 activated aluminosilicate gels. Cem Concr Res 151, 106618.
794 https://doi.org/https://doi.org/10.1016/j.cemconres.2021.106618

795 Moraes, J.C.B., Font, A., Soriano, L., Akasaki, J.L., Tashima, M.M., Monzó, J., Borrachero, M. v, Payá,
796 J., 2018. New use of sugar cane straw ash in alkali-activated materials: A silica source for the
797 preparation of the alkaline activator. Constr Build Mater 171, 611–621.
798 https://doi.org/https://doi.org/10.1016/j.conbuildmat.2018.03.230

799 MORI, H., 2003. Extraction of Silicon Dioxide from Waste Colored Glasses by Alkali Fusion Using
800 Sodium Hydroxide. Journal of the Ceramic Society of Japan 111, 376–381.
801 https://doi.org/10.2109/jcersj.111.376

802 Moukannaa, S., Nazari, A., Bagheri, A., Loutou, M., Sanjayan, J.G., Hakkou, R., 2019. Alkaline fused
803 phosphate mine tailings for geopolymer mortar synthesis: Thermal stability, mechanical and
804 microstructural properties. J Non Cryst Solids 511, 76–85.
805 https://doi.org/https://doi.org/10.1016/j.jnoncrysol.2018.12.031

806 Moutaoukil, G., Alehyen, S., Sobrados, I., Taibi, M., 2022. Microstructural and 29Si and 27Al MAS
807 NMR spectroscopic evaluations of alkali cation and curing effects on Class C fly ash-based
808 geopolymer. Chemical Data Collections 41, 100898.
809 https://doi.org/https://doi.org/10.1016/j.cdc.2022.100898

810 Nedeljković, M., Šavija, B., Zuo, Y., Luković, M., Ye, G., 2018. Effect of natural carbonation on the
811 pore structure and elastic modulus of the alkali-activated fly ash and slag pastes. Constr Build
812 Mater 161, 687–704. https://doi.org/https://doi.org/10.1016/j.conbuildmat.2017.12.005

813 Pangdaeng, S., Sata, V., Aguiar, J.B., Pacheco-Torgal, F., Chindaprasirt, P., 2015. Apatite formation on
814 calcined kaolin–white Portland cement geopolymer. Materials Science and Engineering: C 51,
815 1–6. https://doi.org/https://doi.org/10.1016/j.msec.2015.02.039

816 Passuello, A., Rodríguez, E.D., Hirt, E., Longhi, M., Bernal, S.A., Provis, J.L., Kirchheim, A.P., 2017.
817 Evaluation of the potential improvement in the environmental footprint of geopolymers using

818 waste-derived activators. J Clean Prod 166, 680–689.
819 https://doi.org/https://doi.org/10.1016/j.jclepro.2017.08.007

820 Perez-Cortes, P., Escalante-Garcia, J.I., 2020. Gel composition and molecular structure of alkali-
821 activated metakaolin-limestone cements. Cem Concr Res 137, 106211.
822 https://doi.org/https://doi.org/10.1016/j.cemconres.2020.106211

823 Puertas, F., Torres-Carrasco, M., 2014. Use of glass waste as an activator in the preparation of alkali-
824 activated slag. Mechanical strength and paste characterisation. Cem Concr Res 57, 95–104.
825 https://doi.org/https://doi.org/10.1016/j.cemconres.2013.12.005

826 Puligilla, S., Mondal, P., 2015. Co-existence of aluminosilicate and calcium silicate gel characterized
827 through selective dissolution and FTIR spectral subtraction. Cem Concr Res 70, 39–49.

828 Qian, L.-P., Ahmad, M.R., Lao, J.-C., Dai, J.-G., 2023. Recycling of red mud and flue gas residues in
829 geopolymer aggregates (GPA) for sustainable concrete. Resour Conserv Recycl 191, 106893.
830 https://doi.org/https://doi.org/10.1016/j.resconrec.2023.106893

831 Quina, M.J., Bordado, J.M., Quinta-Ferreira, R.M., 2014. Recycling of air pollution control residues
832 from municipal solid waste incineration into lightweight aggregates. Waste Management 34,
833 430–438. https://doi.org/https://doi.org/10.1016/j.wasman.2013.10.029

834 Rafeet, A., Vinai, R., Soutsos, M., Sha, W., 2019. Effects of slag substitution on physical and
835 mechanical properties of fly ash-based alkali activated binders (AABs). Cem Concr Res 122,
836 118–135. https://doi.org/https://doi.org/10.1016/j.cemconres.2019.05.003

837 Shi, Z., Shi, C., Wan, S., Zhang, Z., 2018. Effects of alkali dosage and silicate modulus on alkali-silica
838 reaction in alkali-activated slag mortars. Cem Concr Res 111, 104–115.
839 https://doi.org/https://doi.org/10.1016/j.cemconres.2018.06.005

840 Shirley, R., Black, L., 2011. Alkali activated solidification/stabilisation of air pollution control residues
841 and co-fired pulverised fuel ash. J Hazard Mater 194, 232–242.
842 https://doi.org/https://doi.org/10.1016/j.jhazmat.2011.07.100

843 Soriano, L., Font, A., Borrachero, M. v, Monzó, J.M., Payá, J., Tashima, M.M., 2022. Biomass ashes to
844 produce an alternative alkaline activator for alkali-activated cements. Mater Lett 308, 131198.
845 https://doi.org/https://doi.org/10.1016/j.matlet.2021.131198

846 Stegemann, J.A., 2014. The potential role of energy-from-waste air pollution control residues in the
847 industrial ecology of cement. J Sustain Cem Based Mater 3, 111–127.

848 Tchakouté, H.K., Bewa, C.N., Fotio, D., Dieuhou, C.M., Kamseu, E., Rüscher, C.H., 2021. Influence of
849 alumina on the compressive strengths and microstructural properties of the acid-based
850 geopolymers from calcined indurated laterite and metakaolin. Appl Clay Sci 209, 106148.
851 https://doi.org/https://doi.org/10.1016/j.clay.2021.106148

852 Torres-Carrasco, M., Puertas, F., 2015. Waste glass in the geopolymer preparation. Mechanical and
853 microstructural characterisation. J Clean Prod 90, 397–408.
854 https://doi.org/https://doi.org/10.1016/j.jclepro.2014.11.074

855 Tu, W., Zhu, Y., Fang, G., Wang, X., Zhang, M., 2019. Internal curing of alkali-activated fly ash-slag
856 pastes using superabsorbent polymer. Cem Concr Res 116, 179–190.
857 https://doi.org/https://doi.org/10.1016/j.cemconres.2018.11.018

858 Turner, L.K., Collins, F.G., 2013. Carbon dioxide equivalent (CO2-e) emissions: A comparison between
859 geopolymer and OPC cement concrete. Constr Build Mater 43, 125–130.
860 https://doi.org/https://doi.org/10.1016/j.conbuildmat.2013.01.023

861 Us, E.P.A., 1992. Toxicity characteristics leaching procedure (TCLP), method 1311.

862 Vinai, R., Soutsos, M., 2019a. Production of sodium silicate powder from waste glass cullet for alkali
863 activation of alternative binders. Cem Concr Res 116, 45–56.
864 https://doi.org/https://doi.org/10.1016/j.cemconres.2018.11.008

865 Vinai, R., Soutsos, M., 2019b. Production of sodium silicate powder from waste glass cullet for alkali
866 activation of alternative binders. Cem Concr Res 116, 45–56.

867 Walkley, B., San Nicolas, R., Sani, M.-A., Rees, G.J., Hanna, J. v, van Deventer, J.S.J., Provis, J.L., 2016.
868 Phase evolution of C-(N)-A-S-H/N-A-S-H gel blends investigated via alkali-activation of synthetic
869 calcium aluminosilicate precursors. Cem Concr Res 89, 120–135.
870 https://doi.org/https://doi.org/10.1016/j.cemconres.2016.08.010

871 Wang, Y., Cao, Y., Zhang, Z., Huang, J., Zhang, P., Ma, Y., Wang, H., 2022. Study of acidic degradation
872 of alkali-activated materials using synthetic C-(N)-A-S-H and N-A-S-H gels. Compos B Eng 230,
873 109510. https://doi.org/https://doi.org/10.1016/j.compositesb.2021.109510

874 Yang, M., Zheng, Y., Li, X., Yang, X., Rao, F., Zhong, L., 2022. Durability of alkali-activated materials
875 with different C–S–H and N-A-S-H gels in acid and alkaline environment. Journal of Materials
876 Research and Technology 16, 619–630.
877 https://doi.org/https://doi.org/10.1016/j.jmrt.2021.12.031

878 Zhang, J., Tan, H., Bao, M., Liu, X., Luo, Z., Wang, P., 2021. Low carbon cementitious materials:
879 Sodium sulfate activated ultra-fine slag/fly ash blends at ambient temperature. J Clean Prod
880 280, 124363. https://doi.org/https://doi.org/10.1016/j.jclepro.2020.124363

881 Zhang, M., Zhao, M., Zhang, G., El-Korchi, T., Tao, M., 2017. A multiscale investigation of reaction
882 kinetics, phase formation, and mechanical properties of metakaolin geopolymers. Cem Concr
883 Compos 78, 21–32.

884 Zhang, S., Duque-Redondo, E., Kostiuchenko, A., Dolado, J.S., Ye, G., 2021. Molecular dynamics and
885 experimental study on the adhesion mechanism of polyvinyl alcohol (PVA) fiber in alkali-
886 activated slag/fly ash. Cem Concr Res 145, 106452.
887 https://doi.org/https://doi.org/10.1016/j.cemconres.2021.106452

888 Zhang, Z., Wang, H., Provis, J.L., Bullen, F., Reid, A., Zhu, Y., 2012. Quantitative kinetic and structural
889 analysis of geopolymers. Part 1. The activation of metakaolin with sodium hydroxide.
890 Thermochim Acta 539, 23–33. https://doi.org/10.1016/J.TCA.2012.03.021

891